

# The Intrinsic Properties of Multiwavelength Energy Spectra for Fermi Teraelectronvolt Blazars

R.X. ZHOU,<sup>1</sup> Y.G. ZHENG,<sup>1</sup> K.R. ZHU,<sup>1</sup> AND S.J. KANG<sup>2</sup>

<sup>1</sup>*Department of Physics, Yunnan Normal University, Kunming, Yunnan, 650092, People's Republic of China*

<sup>2</sup>*School of Physics and Electrical Engineering, Liupanshui Normal University, Liupanshui, Guizhou, 553004, People's Republic of China*

(Received –; Revised –; Accepted –)

Submitted to ApJ

## ABSTRACT

In this paper, we have selected a sample of 64 teraelectronvolt blazars, with redshift, from those classified in the fourth Fermi Large Area Telescope source catalog<sup>a</sup>). We have obtained the values of the relevant physical parameters by performing a log-parabolic fitting of the average-state multiwavelength spectral energy distributions. We estimate the range of the radiation zone parameters, such as the Doppler factor ( $D$ ), the magnetic field strength ( $B$ ), the radiative zone radius ( $R$ ) and the peak Lorentz factor ( $\gamma_p$ ) of nonthermal electrons. Here, we show that (1) there is a strong linear positive correlation between the intrinsic synchrotron peak frequency and the intrinsic inverse Compton scattering (ICs) peak frequency among different types of blazars; (2) if radio bands are excluded, the spectral index of each band is negatively correlated with the intrinsic peak frequency; (3) there is a strong linear negative correlation between the curvature at the peak and the intrinsic peak frequency of the synchrotron bump, and a weak positive correlation between the curvature at the peak and the intrinsic peak frequency of the ICs bump; (4) there is a strong linear positive correlation between the intrinsic ICs peak luminosity and intrinsic  $\gamma$ -ray luminosity and between the intrinsic ICs peak frequency and peak Lorentz factor; (5) there is a strong negative linear correlation between  $\log B$  and  $\log \gamma_p$ ; and (6) there is no correlation between  $\log R$  and  $\log \gamma_p$ .

*Keywords:* Blazars: TeV - gamma rays: galaxies - methods: statistical - radiation mechanisms: non-thermal

## 1. INTRODUCTION

Blazars are one of the most extreme subclasses of active galactic nuclei (AGNs), characterized by high luminosity, high polarization, rapid flux variability, radio core dominance, apparent superluminal motions and strong  $\gamma$ -ray emission (Urry & Padovani 1995; Yang et al. 2014; Fan et al. 2016). Blazars are usually classified as BL Lacertae (BL Lac) objects or flat-spectrum radio quasars (FSRQs). They are distinctive in BL Lac objects characterized by weak or no emission lines (equivalent Width of a line  $\leq 5\text{\AA}$ ) whereas FSRQs show broad, strong emission lines. Their continuous nonthermal radiation is thought to arise from a relativistic jet oriented in the direction of the observer (Ghisellini et al. 1986). The beaming effect is significant to the observational properties of blazars (Fan et al. 2013a; Lin et al. 2017) and embodies the relativistic property of a jet. The Doppler factors of most objects have been estimated in literature (Lähteenmäki & Valtaoja 1999; Hovatta et al. 2009; Fan et al. 2013b, 2014; Lin et al. 2017).

The multiwavelength spectral energy distribution (SED) of BL Lac objects generally displays a double broad bump structure in the  $\log \nu - \log \nu f_\nu$  frame (Kang et al. 2018; Lin & Fan 2018; Zhang & Fan 2019; Costamante 2020). The low-energy bump is located in the range of radio to X-ray frequencies, which is generally believed to be generated by the synchrotron radiation of extreme relativistic electrons in the jet. However, the high-energy bump is located in the frequency range of megaelectronvolts to giga-electronvolts, and its generation mechanism remains an outstanding

Corresponding author: Y.G. Zheng  
yzzyg@ynu.edu.cn

<sup>a</sup>) [https://fermi.gsfc.nasa.gov/ssc/data/access/lat/8yr\\_catalog/](https://fermi.gsfc.nasa.gov/ssc/data/access/lat/8yr_catalog/)

issue. Within the lepton origin model, the high-energy bump is generated by the inverse Compton scattering (ICs) process of the extreme relativistic electron. If the soft photons scattered on the inverse Compton come from the synchrotron radiation soft photons inside the jet, the process is known as the synchrotron self-Compton (SSC) process (Maraschi et al. 1992; Mastichiadis & Kirk 1997; Fossati et al. 1998; Kang et al. 2018; Zheng et al. 2019). At present, the SSC model is able to explain the multiwavelength SED of blazars very well and SSC is generally considered to be the dominant factor in  $\gamma$ -ray radiation (Fossati et al. 1998; Zheng et al. 2019). Based on a nonthermal relativistic electron energy distribution (EED), we can reproduce the multiwavelength SED of blazars by the SSC model (Zheng et al. 2018, 2019, 2020). It is a significant research topic that links the parameters corresponding to the observation to the parameters corresponding to the radiation region of the jet.

Different SEDs are produced by different particle distributions in the jet radiation region of blazars. The photon spectrum of the blazars depends on the electron spectrum, which is directly related to the physical conditions and processes in the radiation region of the jet. Therefore, we can determine the EED form from the observed photon spectrum. The study of SED properties is essential to theoretical models and we can obtain important information related to the physical properties of the radiation region through the parameters. The shape and position of the two bumps of the SED in the  $\log \nu - \log \nu f_\nu$  coordinate system and the mechanism that controls them have been a subject of discussion for some years. Abdo et al. (2010) proposed that the synchrotron peak frequency  $\nu_{\text{peak}}^{\text{syn}}$  could be estimated by effective spectral indices  $\alpha_{\text{ox}}$  and  $\alpha_{\text{ro}}$ , and gave the empirical relations. Fan et al. (2016) presented a least-squares fitting method to estimate the peak frequency  $\nu_{\text{peak}}^{\text{syn}}$  by fitting the broadband SED, and the parameters of the spectral curvature and the peak flux were also obtained. Zheng et al. (2021) used an extrapolation model to estimate the peak location of the synchrotron SED component. According to the observation results of the peak frequency of the synchrotron SED component, BL Lac objects could be classified as either low- or high-frequency-peaked (Padovani & Giommi 1995); more recently they have been classified as low-synchrotron-peaked (LBLs; e.g.,  $\nu_{\text{peak}}^{\text{syn}} < 10^{14}\text{Hz}$ ), intermediate-synchrotron-peaked (IBLs; e.g.,  $10^{14} < \nu_{\text{peak}}^{\text{syn}} < 10^{15}\text{Hz}$ ), or high-synchrotron-peaked (HBLs, e.g.,  $\nu_{\text{peak}}^{\text{syn}} > 10^{15}\text{Hz}$ ) sources (Abdo et al. 2010).

Curvature is a critical spectral parameter that can provide important information enabling us to study particle acceleration mechanisms. Tramacere et al. (2011) presented the statistical acceleration case, using the multiplicative model of the central limit theorem to generate the EED in the form of a logarithmic parabola. It consists of two mechanisms: energy-dependent acceleration probability and fluctuation of fractional acceleration gain. The energy distribution of the electrons produced by the former is

$$\log \left( \frac{N_e(\gamma)}{\text{cons.}} \right) = -r \log^2 \left( \frac{\gamma}{\gamma_0} \right) - s \log \left( \frac{\gamma}{\gamma_0} \right) \quad (1)$$

where  $\gamma_0$  is the initial electron Lorentz factor,  $r = q/(2 \log \varepsilon)$  is the EED curvature term,  $s = -2r/q \log(g/\gamma_0) - (q-2)/2$ , and  $\varepsilon = \text{cons.}$  is constant.  $p_a = g/\gamma^q$  denotes the energy-dependent acceleration probabilities. The energy distribution of the electrons produced by the latter is

$$\log \left( \frac{N_e(\gamma)}{G} \right) = -\frac{c_e}{2\sigma_\gamma^2} \log^2 \left( \frac{\gamma}{\gamma_0} \right) - (\mu/\sigma_\gamma^2 - 1) \log \left( \frac{\gamma}{\gamma_0} \right) \quad (2)$$

where  $G = 10^{K - \log \gamma_0 - \mu^2/(2c_e\sigma_\gamma^2)}$  is a constant term,  $c_e = 1/\log_{10} e$  is the logarithm conversion constant,  $\sigma_\gamma^2 \approx n_s(\sigma_\varepsilon/\bar{\varepsilon})^2$ ,  $\mu = n_s[c_e \log \bar{\varepsilon} - (\sigma_\varepsilon/\bar{\varepsilon})^2/2]$ , and the coefficient of the second term can be defined through the curvature term of the EED:  $r = c_e/(2\sigma_\gamma^2)$ .

The data of the fourth Fermi Large Area Telescope (LAT) Source Catalog (4FGL), which is by far the largest sample of  $\gamma$ -ray sources, has been released. There are a total of 5064  $\gamma$ -ray sources in 4FGL catalog<sup>1</sup> (Abdollahi et al. 2020). Based on 4FGL, the fourth catalog of AGN data<sup>2</sup> (4LAC) has been released (Ajello et al. 2020). The 4LAC catalog contains 3207  $\gamma$ -ray sources: 2863 high Galactic latitude ( $|b| > 10^\circ$ ) and 344 low Galactic latitude ( $|b| \leq 10^\circ$ )  $\gamma$ -ray sources, most of which (3137) appertain to blazars (Ajello et al. 2020). The blazars in 4LAC catalog include 694 FSRQs, 1131 BL Lac objects, and 1312 blazar candidates of uncertain type (BCUs). In addition to the 4LAC, we can collect a large amount of multiband data from Space Science Data Center (SSDC<sup>3</sup>) and the NASA/IPAC Extragalactic

<sup>1</sup> [https://fermi.gsfc.nasa.gov/ssc/data/access/lat/8yr\\_catalog/gll\\_psc\\_v21.fit](https://fermi.gsfc.nasa.gov/ssc/data/access/lat/8yr_catalog/gll_psc_v21.fit)

<sup>2</sup> <https://doi.org/10.3847/1538-4357/ab791e>

<sup>3</sup> <https://tools.ssdsc.asi.it/SED/>

Database (NED<sup>4</sup>) covering the range of radio to  $\gamma$ -ray bands. These samples provide new opportunities and challenges for the study of the multiwavelength radiation characteristics and spectral shapes of Fermi blazars.

At present, for the very high energy (VHE;  $E > 0.1\text{TeV}$ )  $\gamma$ -ray (TeV) band, 228 extragalactic objects can be obtained from the online TeVCat catalog<sup>5</sup>, which has been compiled from observations by ground-based telescopes (Wakely & Horan 2008). The radiation of 186 of these sources in the gigaelectronvolt energy band has been detected by Fermi-LAT; 73 of these are TeV blazars (Abdollahi et al. 2020). These blazars include 62 TeV BL Lac objects, 7 TeV FSRQs, and 4 BCUs. TeV sources are bright and although rare, they play a crucial role in the study of high-energy (or VHE) radiation mechanisms and spectral shapes, extragalactic background light, and intergalactic magnetic fields (Finke et al. 2010; Ackermann et al. 2012; Fallah Ramazani et al. 2017).

In recent years, with the increase of the number of TeV sources, some researchers have studied their energy spectrum structure and discussed the differences in the multiwavelength spectrum shapes of different source types (Zhang et al. 2012; Chen 2014; Lin & Fan 2016, 2018; Kang et al. 2018; Zhong et al. 2018; Zhang & Fan 2019). In this work, we have collected the average-state multifrequency data based on all 73 TeV blazars in 4LAC and fit the SED with the log-parabolic model to obtain the relevant physical parameters. Our objective is to summarize the differences in the multiwavelength radiation characteristics of HBLs, IBLs, LBLs, and FSRQs through statistical analysis of sample parameters and to estimate the parameters of the jet radiation zone. The paper is structured as follows: In Section 2, we introduce the fitting model and parameters. In Section 3, we give the sample and data processing. In Section 4, the results are given. In Section 5, the discussion and conclusion are presented. Throughout the paper, we assume the Hubble constant to be  $H_0 = 75 \text{ km s}^{-1} \text{ Mpc}^{-1}$ , the matter energy density to be  $\Omega_M = 0.27$ , the radiation energy density to be  $\Omega_r = 0$ , and the dimensionless cosmological constant to be  $\Omega_\Lambda = 0.73$ .

## 2. THE MODELS AND PARAMETERS

### 2.1. The log-parabolic model

It is worth noting that we can employ a reasonably smooth interpolation (or extrapolation) model to estimate the peak frequency of the two bumps of the SED component (Massaro et al. 2004a; Błażejowski et al. 2005; Tramacere et al. 2009; Ushio et al. 2010; Zheng et al. 2021). Based on this method, we can also obtain the curvature of the energy spectrum, the spectral index of a given frequency, and the peak luminosity.

In the  $\nu - f_\nu$  frame, we introduce a log-parabolic model with (Baloković et al. 2016)

$$f(\nu) = k \left( \frac{\nu}{\nu_*} \right)^{-\alpha_* - \beta \log(\nu/\nu_*)} \quad (3)$$

where  $\alpha_*$  and  $\beta$  are free parameters,  $\nu_*$  is the reference frequency,  $\alpha_*$  equals the local power-law photon index, and  $\beta$  is the curvature of the energy spectral bump, which represents the deviation of the spectral slope away from  $\nu_*$  (Zheng et al. 2021). This expression can be written as

$$\log \nu f_\nu = \hat{A}(\log \nu)^2 + \hat{B} \log \nu + \hat{C} \quad (4)$$

in the  $\log \nu - \log \nu f_\nu$  frame. In this expression,  $\hat{A} = -\beta$ ,  $\hat{B} = 1 - \alpha_* + 2\beta \log \nu_*$ , and  $\hat{C} = \log k + \alpha_* \log \nu_* - \beta(\log \nu_*)^2$ .

Generally, nonthermal radiation of blazars can be described by a typical power law:

$$f_\nu \propto \nu^{-\alpha} \quad (5)$$

where  $f_\nu$  is the flux at frequency  $\nu$  and  $\alpha$  is the spectral index (Fan et al. 2016). By transformation of Equation (5) into  $\log \nu - \log \nu f_\nu$  frame, we can obtain the relation

$$\log \nu f_\nu = k + (1 - \alpha) \log \nu \quad (6)$$

where  $k$  is a constant. Comparing Equation (4) and Equation (6), we find that at  $\nu = \nu_0$ , their slope values are equal, that is,

$$\left[ \frac{d(\log \nu f_\nu)}{d(\log \nu)} \right]_{\nu=\nu_0} = 2\hat{A}(\log \nu_0) + \hat{B} = 1 - \alpha \quad (7)$$

<sup>4</sup> <http://ned.ipac.caltech.edu/>

<sup>5</sup> <http://tevcat.uchicago.edu/>

Thus, the spectral index at frequency  $\nu_0$  is

$$\alpha = 1 - [2\hat{A}(\log \nu_0) + \hat{B}] \quad (8)$$

and the peak frequency of the synchrotron bump and of the ICs bump is

$$\log \nu_{\text{peak}} = -\frac{\hat{B}}{2\hat{A}} \quad (9)$$

Based on the definition of the curvature term of the EED in Equation (1) and Equation (2), we can estimate the energy spectral curvature of the synchrotron bump and of the ICs bump at the peak as

$$\beta = -\hat{A} \quad (10)$$

The peak flux can be calculated as

$$f_{\text{peak}} = k \left( \frac{\nu_{\text{peak}}}{\nu_*} \right)^{-\alpha_* - \beta \log(\nu_{\text{peak}}/\nu_*)} \quad (11)$$

and the peak luminosity can be calculated as

$$L_{\text{peak}} = 4\pi d_L^2 \nu_{\text{peak}} f_{\text{peak}} \quad (12)$$

where  $d_L$  is the luminosity distance (Fan et al. 2015, 2016, 2017).

Equation (4) is just a phenomenological fit of the data, which does not take into account the internal physical mechanisms due to injection and the cooling effects. Here, we focus only on the statistical and physical significance of the fitting parameters.

## 2.2. The intrinsic physical parameters

To obtain the intrinsic physical parameters, we need to transform them from the observer's coordinate system into the co-moving coordinate system, to introduce Doppler corrections and redshift corrections (Kembhavi & Narlikar 1999). The intrinsic physical parameters are described by the equations (Xie et al. 2001; Fan et al. 2013a, 2015):

$$\nu' = \frac{(1+z)}{D} \nu \quad (13)$$

$$f'(\nu') = (1+z)^{\alpha_\nu - 1} \left( \frac{1}{D} \right)^{(3+\alpha_\nu)} f(\nu) \quad (14)$$

$$L'(\nu') = (1+z)^{\alpha_\nu} \left( \frac{1}{D} \right)^{(4+\alpha_\nu)} L(\nu) \quad (15)$$

where the physical quantities with a prime are calculated in the co-moving frame and the observed quantities are without a prime. The spectral index  $\alpha_\nu$  is estimated according to the method in Section 2.1.

In order to further analyze the physical mechanism and obtain essential radiation parameters, we relate the electron spectrum parameters to the photon spectrum parameters obtained, as in Section 2.1 (Massaro et al. 2006; Paggi et al. 2009, 2011; Chen 2014; Fan et al. 2016; Chen 2018). In the Thomson scattering region, we have (See Appendix A for details)

$$\left\{ \begin{array}{l} D_{\text{Th}} = (247.2179)^{\frac{1}{4\xi}} (1+z)^{\frac{1-\xi}{\xi}} \left( \frac{10^{45} \text{erg s}^{-1}}{L_{\text{peak,Th}}^{\text{ic}}} \right)^{\frac{1}{4\xi}} \left( \frac{L_{\text{peak}}^{\text{syn}}}{10^{45} \text{erg s}^{-1}} \right)^{\frac{1}{2\xi}} \\ \quad \times \left( \frac{\nu_{\text{peak,Th}}^{\text{ic}}}{10^{23} \text{Hz}} \right)^{\frac{1}{2\xi}} \left( \frac{10^{15} \text{Hz}}{\nu_{\text{peak}}^{\text{syn}}} \right)^{\frac{1}{\xi}} \left( \frac{1 \text{day}}{\Delta t} \right)^{\frac{1}{2\xi}} (\beta_{\text{syn}})^{\frac{1}{8\xi}} \\ B = 13.4109 \left( \frac{\nu_{\text{peak}}^{\text{syn}}}{10^{15} \text{Hz}} \right)^2 \left( \frac{10^{23} \text{Hz}}{\nu_{\text{peak,Th}}^{\text{ic}}} \right) \\ R = 2.7235 \times 10^{16} \left( \frac{\nu_{\text{peak,Th}}^{\text{ic}}}{10^{23} \text{Hz}} \right) \left( \frac{10^{15} \text{Hz}}{\nu_{\text{peak}}^{\text{syn}}} \right)^2 \left( \frac{L_{\text{peak}}^{\text{syn}}}{10^{45} \text{erg s}^{-1}} \right) \left( \frac{10^{45} \text{erg s}^{-1}}{L_{\text{peak,Th}}^{\text{ic}}} \right)^{\frac{1}{2}} \\ \gamma_{\text{p}} = 8660.3 \left( \frac{\nu_{\text{peak,Th}}^{\text{ic}}}{10^{23} \text{Hz}} \cdot \frac{10^{15} \text{Hz}}{\nu_{\text{peak}}^{\text{syn}}} \right)^{\frac{1}{2}} 10^{-\frac{1}{10\beta_{\text{syn}}}} \end{array} \right. \quad (16)$$

In the Klein-Nishina (KN) scattering region, we have

$$\left\{ \begin{array}{l} D_{\text{KN}} = (0.0295)^{\frac{1}{\zeta}} (1+z)^{\frac{\zeta-2}{\zeta}} \left( \frac{L_{\text{peak}}^{\text{syn}}}{10^{45} \text{ erg s}^{-1}} \right)^{\frac{1}{\zeta}} \left( \frac{10^{45} \text{ erg s}^{-1}}{L_{\text{peak,KN}}^{\text{ic}}} \right)^{\frac{1}{2\zeta}} \\ \quad \times \left( \frac{10^{15} \text{ Hz}}{\nu_{\text{peak}}^{\text{syn}}} \right)^{\frac{3}{2\zeta}} \left( \frac{\nu_{\text{peak,KN}}^{\text{ic}}}{10^{23} \text{ Hz}} \right)^{\frac{1}{\zeta}} \left( \frac{1 \text{ day}}{\Delta t} \right)^{\frac{1}{\zeta}} 10^{\frac{2}{5\beta_{\text{syn}}\zeta}} (\beta_{\text{syn}})^{-\frac{1}{4\zeta}} \\ B = 1.5356 \times 10^3 \left( \frac{\nu_{\text{peak}}^{\text{syn}}}{10^{15} \text{ Hz}} \right) \left( \frac{10^{23} \text{ Hz}}{\nu_{\text{peak,KN}}^{\text{ic}}} \right)^2 10^{-\frac{2}{5\beta_{\text{syn}}}} \\ R = 7.6456 \times 10^{13} (\beta_{\text{syn}})^{-\frac{1}{4}} 10^{\frac{2}{5\beta_{\text{syn}}}} \left( \frac{\nu_{\text{peak,KN}}^{\text{ic}}}{10^{23} \text{ Hz}} \right) \left( \frac{10^{15} \text{ Hz}}{\nu_{\text{peak}}^{\text{syn}}} \right)^{\frac{3}{2}} \left( \frac{L_{\text{peak}}^{\text{syn}}}{10^{45} \text{ erg s}^{-1}} \right) \left( \frac{10^{45} \text{ erg s}^{-1}}{L_{\text{peak,KN}}^{\text{ic}}} \right)^{\frac{1}{2}} \\ \gamma_{\text{p}} = 809.332 \left( \frac{\nu_{\text{peak,KN}}^{\text{ic}}}{10^{23} \text{ Hz}} \right) 10^{\frac{1}{10\beta_{\text{syn}}}} \end{array} \right. \quad (17)$$

where  $D$  is the Doppler factor;  $\gamma_{\text{p}}$  is the peak Lorentz factor of nonthermal electrons;  $R$  is the radius of the emission region in centimeters,  $B$  is the magnetic field of the jet in gauss;  $z$  is the redshift;  $\nu_{\text{peak}}^{\text{syn}}$  and  $\nu_{\text{peak}}^{\text{ic}}$  are the peak frequencies of synchrotron radiation and the inverse Compton spectrum, respectively, in hertz;  $L_{\text{peak}}^{\text{syn}}$  and  $L_{\text{peak}}^{\text{ic}}$  are, respectively, the peak luminosity of synchrotron radiation and the inverse Compton energy spectrum in ergs per second;  $\beta_{\text{syn}}$  is the energy spectral curvature of the synchrotron bump;  $\xi = 1 + \frac{2\alpha_{\nu_{\text{peak}}^{\text{syn}}} - \alpha_{\nu_{\text{peak}}^{\text{ic}}}}{4}$ ,  $\zeta = \frac{5+2\alpha_{\nu_{\text{peak}}^{\text{syn}}} - \alpha_{\nu_{\text{peak}}^{\text{ic}}}}{2}$ ;  $\alpha_{\nu_{\text{peak}}} = -\frac{\partial \log f_{\nu}}{\partial \log \nu} = 1$  denotes the spectral indices at the peak frequency; and  $\Delta t$  is the variability timescale. For simplicity, we use the average value of variability timescale,  $\frac{\Delta t}{(1+z)} \approx 1$  day, in the source frame (Ulrich et al. 1997; Abdo et al. 2010; Nalewajko 2013; Kang et al. 2014; Zhang et al. 2015; Chen 2018).

Through the log-parabolic model fitting, 12 fitting parameters can be obtained as  $\beta_{\text{syn}}$ ,  $\beta_{\text{ic}}$ ,  $\log \nu_{\text{peak}}^{\text{syn}}$ ,  $\log \nu_{\text{peak}}^{\text{ic}}$ ,  $\log L_{\text{peak}}^{\text{syn}}$ ,  $\log L_{\text{peak}}^{\text{ic}}$ , and the spectral index  $\alpha_{\nu}$  of each band: the radio (1.4 GHz), infrared (2.2  $\mu\text{m}$ ), optical (J band, 1250 nm), ultraviolet (250 nm), soft X-ray (1 keV) and  $\gamma$ -ray (20 GeV) bands (Fossati et al. 1998; Nie et al. 2014; Yang et al. 2017). We can also calculate the physical parameters indirectly, including  $D$ ,  $R$ ,  $B$  and  $\gamma_{\text{p}}$ . In addition, we can calculate the  $\gamma$ -ray luminosity at  $E = 20$  GeV by the following formula (Fan et al. 2012, 2015; Nie et al. 2014; Yang et al. 2017):

$$L(E) = 4\pi d_L^2 \nu f(E) \quad (18)$$

where  $f(E)$  is the  $\gamma$ -ray flux density, which can be expressed as (Nie et al. 2014; Yang et al. 2017)

$$f(E) = 6.626 \times 10^{-4} \frac{1-\Gamma}{E_U^{1-\Gamma} - E_L^{1-\Gamma}} \cdot N \cdot E^{1-\Gamma} \quad (\text{Jy}) \quad (19)$$

where  $N = N_0 \frac{E_U^{1-\Gamma} - E_L^{1-\Gamma}}{1-\Gamma}$  is the integral photon flux in units of photon count per square centimeter per second, which can be obtained from 4FGL.  $\Gamma$  is the  $\gamma$ -ray photon spectrum index, and  $E_L = 1$  GeV and  $E_U = 100$  GeV are the lower and the upper integrating limits.

### 3. SAMPLE SELECTION AND DATA PROCESSING

The 4LAC samples list 3137  $\gamma$ -ray blazars (Ajello et al. 2020) with 694 FSRQs, 1131 BL Lac objects, and 1312 BCUs. We selected all 73 Fermi TeV blazars from the 4LAC samples, including 65 blazars with redshift values. In this sample, there are 57 TeV BL Lac objects with redshifts, 7 TeV FSRQs with redshifts and 1 TeV BCU with redshifts (Ajello et al. 2020).

In order to reasonably estimate the physical parameters and obtain an accurate energy spectrum distribution diagram, we collected a large number of multifrequency data from the SSDC<sup>6</sup> database and 4FGL, respectively, including the flux density and the flux densities error of the radio, infrared, optical, ultraviolet, soft X-ray, and  $\gamma$ -ray bands (Aharonian et al. 2001; H. E. S. S. Collaboration et al. 2010; HESS Collaboration et al. 2013; Abramowski et al. 2015; Biteau & Williams 2015; Sharma et al. 2015; Lin & Fan 2018; Zhang & Fan 2019; Abdollahi et al. 2020). In the calculation, we grouped and filtered the SED observation data of each source as follows: (1) For multiple data points of the same frequency, we took the average value of the corresponding flux. For the flux without error, we took 1% of

<sup>6</sup> The SSDC SED Builder contains radio to TeV band data from several missions and experiments together with catalogs and archival data, such as the NED, the DB database (including CLASSCAT, Fermi1FGL, 2FGL, MAGIC, VERITAS, and IPC), TOMASS data, and USNOA2 data.

the observed radio and optical flux, 2% of the observed ultraviolet and X-ray flux, and 20% of the observed  $\gamma$ -ray flux as the errors of the data points whose errors were available (Zhang et al. 2012; Aleksić et al. 2014; Zheng et al. 2017; Lin & Fan 2018). (2) Since NED collected observations using very different methods and literature from those used by other databases, we removed the data whose  $\nu > 10^{16}$  Hz from NED according to Lin & Fan (2018). (3) Data with the upper limit of energy, duplicates, and flux errors greater than the flux value were excluded. (4) We considered that in the ultraviolet (or optical) band, some SEDs of AGNs may have a bump formed by tori, accretion disks, or host galaxies (the bump of thermal radiation). For this part of the sample,  $13.5 < \log \nu < 15$  observations were ignored for SED processing (Shields 1978; Czerny & Elvis 1987; Giommi et al. 2012; Zhang & Fan 2019).

In our sample, the log-parabolic model was used to fit the average-state multifrequency SED of 65 TeV blazars. Since the log-parabolic shape held only close to the peak of the SED, we repeatedly adjusted the parameters according to Equation (4), so that the reduced chi-square value of each source was close to 0 when fitting the data. The sample data and fitting results are shown in Table 1. Figures 1 and 2 show the SED fitting diagram. In Table 1, Column (1) gives both the 4FGL source name and the TeVCat name. Column (2) gives the class designation for the source and the redshift ( $z$ ), where class represents the type of sample: H, I, L, F and B represent sources belonging to HBLs, IBLs, LBLs, FSRQs, and BCUs, respectively. Column (3) gives the energy spectral curvature of the synchrotron bump and ICs bump at the peak:  $\beta_{\text{syn}}$  and  $\beta_{\text{ic}}$ . Column (4) gives the synchrotron peak frequency and ICs peak frequency in units of hertz:  $\log \nu_{\text{peak}}^{\text{syn}}$  and  $\log \nu_{\text{peak}}^{\text{ic}}$ . Column (5) gives the spectral indices in the radio (1.4GHz) and infrared (2.2 $\mu\text{m}$ ) bands:  $\alpha_{\text{r}}$  and  $\alpha_{\text{ir}}$ . Column (6) gives the spectral indices in the optical (1250nm) and ultraviolet (250nm) bands:  $\alpha_{\text{o}}$  and  $\alpha_{\text{uv}}$ . Column (7) gives the spectral indices in the soft X-ray (1 keV) and  $\gamma$ -ray (20 GeV) bands:  $\alpha_{\text{x}}$  and  $\alpha_{\gamma}$ . Column (8) gives the synchrotron peak luminosity and ICs peak luminosity in units of ergs per second:  $\log L_{\text{peak}}^{\text{syn}}$  and  $\log L_{\text{peak}}^{\text{ic}}$ . Column (9) gives the radio Doppler factor  $D_{\text{r}}$  and  $\gamma$ -ray luminosity  $\log L_{\gamma}$  (20 GeV) in units of ergs per second; the radio Doppler factor ( $D_{\text{r}}$ ) was collected from the following literature: Fan et al. (2013a), Fan et al. (2013b), Fan et al. (2009), Fan et al. (2014), Fan et al. (2017), Lin et al. (2017), Hovatta et al. (2009), Ghisellini et al. (1993), Huang et al. (1999), Wu et al. (2007), Savolainen et al. (2010), Lähteenmäki & Valtaoja (1999), and Wu et al. (2009). Column (10) gives the reduced  $\chi^2$  values for the energy spectrum of the synchrotron bump and the energy spectrum of

the ICs bump of our fits:  $\chi_{\text{syn}}^2$  and  $\chi_{\text{ic}}^2$ , which can be calculated by  $\chi^2 = \frac{1}{N-dof} \sum_{i=1}^N (\hat{y}_i - y_i)^2$ , where  $N$  is the number of observed data points;  $dof$  is the degrees of freedom, i.e., the number of free parameters used for the model; The  $\hat{y}_i$  denotes the expected values from the model; and  $y_i$  denotes the observed data (Ivezić et al. 2014; Massaro et al. 2004a). In addition,  $\sigma$  represents the uncertainty of the parameter in Table 1, which can be calculated by the error transfer formula

according to the equation (Feigelson & Babu 2012), i.e.,  $\sigma(y) = \sqrt{\sum_{i=1}^m \left(\frac{\partial y}{\partial x_i}\right)^2 (\sigma(x_i))^2 + 2 \sum_{i,j=1, i \neq j}^m \frac{\partial y}{\partial x_i} \frac{\partial y}{\partial x_j} \rho_{ij} \sigma(x_i) \sigma(x_j)}$ ,

where  $\rho_{ij}$  is the correlation coefficient.

Based on the calculation results of the synchrotron radiation peak frequency (Equation (10)), we further classified the TeV blazars. The sources were classified as LBLs (i.e.,  $\nu_{\text{peak}}^{\text{syn}} < 10^{14}$ Hz), IBLs (i.e.,  $10^{14} < \nu_{\text{peak}}^{\text{syn}} < 10^{15}$ Hz), HBLs (i.e.,  $\nu_{\text{peak}}^{\text{syn}} > 10^{15}$ Hz), or FSRQs according to Abdo et al. (2010). There was only one source, PGC 2402248, classified as a BCU in our sample, which had little impact on the statistical results, so we removed it in our correlation test and regression analysis.

According to the fitting results in Table 1, we can use Equations (16) and (17) to estimate the physical parameters of the jet radiation zone of the TeV blazars, and the results are listed in Table 2.

#### 4. RESULTS

In our samples of 64 identified classified TeV blazars with redshift, there are 57 BL Lac objects and 7 FSRQs. According to the peak frequency of synchrotron radiation, the sample can be further divided into 46 HBLs, 6 IBLs, 5 LBLs, and 7 FSRQs. Among these, the FSRQs are all low-synchrotron-peaked. Based on our sample, the statistical results of the fitting parameters are listed in Table 3. The histogram distributions of  $\log D$  are shown in Figure 3, where three different definitions of the Doppler factor are represented. Figures 4– 6 show the statistical histograms of the radiation parameters obtained under the KN scattering region conditions between the different types of TeV blazars. The correlation between the parameters and the linear regression analysis results are shown in Table 4.

According to our results, we can infer the following: (1) The spectral index increases gradually from the infrared to the high-energy band in the synchrotron regions and the spectral index is different for different types of TeV blazars. The mean spectral indices obtained are as follows:  $\langle \alpha_{\text{r}} \rangle_{\text{BLLacs}} = -0.19$ ,  $\langle \alpha_{\text{ir}} \rangle_{\text{BLLacs}} = 0.95$ ,  $\langle \alpha_{\text{o}} \rangle_{\text{BLLacs}} = 1.01$ ,

Table 1. Sample Data and Fitting Results

4FGL Name	class	$\beta_{\text{syn}}/(\sigma \times 10^{-4})$	$\log \nu_{\text{peak}}^{\text{syn}}/\sigma$	$\alpha_{\text{r}}/\sigma$	$\alpha_{\text{o}}/\sigma$	$\alpha_{\text{x}}/\sigma$	$\log L_{\text{peak}}^{\text{syn}}/\sigma$	$D_{\text{r}}$	$\chi_{\text{syn}}^2$
Other Name	z	$\beta_{\text{ic}}/(\sigma \times 10^{-4})$	$\log \nu_{\text{peak}}^{\text{ic}}/\sigma$	$\alpha_{\text{i}}/\sigma$	$\alpha_{\text{uv}}/\sigma$	$\alpha_{\text{g}}/\sigma$	$\log L_{\text{peak}}^{\text{ic}}/\sigma$	$\log L_{\text{r}}/\sigma$	$\chi_{\text{ic}}^2$
(1)	(2)	(3)	(4)	(5)	(6)	(7)	(8)	(9)	(10)
J0013.9-1854	H	0.07 / 2.63	16.91 / 0.12	-0.03 / 0.01	0.67 / 0.01	1.08 / 0.02	43.90 / 0.17		0.11
SHBL J001355.9 - 185406	0.095	0.25 / 2.38	24.22 / 0.04	0.63 / 0.01	0.76 / 0.02	1.23 / 0.02	43.26 / 0.06	42.94 / 0.85	0.33
J0033.5-1921	H	0.10 / 0.92	15.81 / 0.03	-0.33 / 0.01	0.72 / 0.01	1.33 / 0.01	45.81 / 0.04	6.43	0.01
KUV 00311 - 1938	0.610	0.24 / 0.60	24.58 / 0.01	0.67 / 0.01	0.85 / 0.01	1.05 / 0.01	45.85 / 0.02	45.83 / 1.44	0.02
J0112.1+2245	I	0.12 / 2.24	14.41 / 0.05	-0.27 / 0.01	1.00 / 0.01	1.74 / 0.01	45.21 / 0.07	9.10	0.08
S2 0109 + 22	0.265	0.10 / 0.45	23.56 / 0.02	0.93 / 0.01	1.16 / 0.01	1.22 / 0.01	45.26 / 0.03	45.22 / 1.69	0.01
J0152.6+0147	H	0.07 / 1.23	16.25 / 0.05	-0.05 / 0.01	0.72 / 0.01	1.18 / 0.01	43.76 / 0.07	3.00	0.02
RGB J0152 + 017	0.080	0.22 / 0.87	24.75 / 0.02	0.69 / 0.01	0.83 / 0.01	0.97 / 0.01	43.64 / 0.03	43.30 / 1.15	0.09
J0214.3+5145	H	0.06 / 1.33	16.50 / 0.07	0.16 / 0.01	0.76 / 0.01	1.11 / 0.01	43.39 / 0.10		0.04
TXS 0210 + 515	0.049	0.66 / 5.06	24.27 / 0.03	0.73 / 0.01	0.84 / 0.01	1.55 / 0.04	43.15 / 0.05	42.64 / 0.94	1.30
J0221.1+3556	F	0.09 / 8.68	13.98 / 0.06	0.14 / 0.03	1.07 / 0.04	1.62 / 0.05	45.75 / 0.08		0.04
S3 0218 + 35	0.944	0.08 / 0.81	21.96 / 0.04	1.03 / 0.03	1.20 / 0.04	1.46 / 0.01	46.69 / 0.05	46.20 / 1.71	0.04
J0222.6+4302	I	0.09 / 1.98	14.65 / 0.06	0.05 / 0.01	0.95 / 0.01	1.49 / 0.01	45.77 / 0.09	0.10	0.11
3C 66A	0.444	0.16 / 0.86	23.37 / 0.02	0.91 / 0.01	1.07 / 0.01	1.41 / 0.01	46.24 / 0.03	46.10 / 1.84	0.06
J0232.8+2018	H	0.05 / 1.60	17.67 / 0.09	0.08 / 0.01	0.65 / 0.01	0.98 / 0.01	44.29 / 0.13	2.50	0.07
1ES 0229 + 200	0.139	0.25 / 1.29	25.20 / 0.02	0.62 / 0.01	0.72 / 0.01	0.75 / 0.01	44.01 / 0.03	43.44 / 0.75	0.16
J0238.4-3116	H	0.06 / 1.29	16.95 / 0.06	0.01 / 0.01	0.67 / 0.01	1.07 / 0.01	44.92 / 0.09		0.03
1RXS J023832.6 - 311658	0.233	0.15 / 1.93	24.23 / 0.06	0.64 / 0.01	0.76 / 0.01	1.13 / 0.02	44.28 / 0.08	44.43 / 1.21	0.24
J0303.4-2407	H	0.07 / 3.38	15.40 / 0.14	0.15 / 0.01	0.86 / 0.02	1.28 / 0.02	45.13 / 0.19		0.14
PKS 0301 - 243	0.266	0.12 / 0.36	24.15 / 0.01	0.83 / 0.01	0.96 / 0.02	1.13 / 0.01	45.16 / 0.02	45.23 / 1.61	0.02
J0319.8+1845	H	0.08 / 1.23	16.37 / 0.05	-0.20 / 0.01	0.67 / 0.01	1.18 / 0.01	44.46 / 0.06		0.05
RBS 0413	0.190	0.47 / 5.75	25.41 / 0.06	0.63 / 0.01	0.79 / 0.01	0.32 / 0.05	44.29 / 0.08	44.02 / 0.94	2.61
J0349.4-1159	H	0.06 / 1.73	17.94 / 0.09	-0.06 / 0.01	0.57 / 0.01	0.95 / 0.01	44.81 / 0.13		0.13
1ES 0347 - 121	0.188	0.27 / 1.57	25.18 / 0.03	0.54 / 0.01	0.66 / 0.01	0.73 / 0.01	44.21 / 0.04	43.76 / 0.84	0.31
J0416.9+0105	H	0.07 / 1.31	17.12 / 0.06	-0.05 / 0.01	0.64 / 0.01	1.05 / 0.01	45.15 / 0.09	2.90	0.04
1ES 0414 + 009	0.287	0.36 / 1.83	24.59 / 0.02	0.61 / 0.01	0.73 / 0.01	1.07 / 0.02	44.61 / 0.03	44.41 / 1.04	0.36
J0449.4-4350	H	0.09 / 3.48	15.58 / 0.10	-0.18 / 0.01	0.78 / 0.02	1.35 / 0.02	45.35 / 0.15		0.15
PKS 0447 - 439	0.205	0.37 / 1.05	24.20 / 0.01	0.73 / 0.01	0.91 / 0.02	1.36 / 0.01	45.52 / 0.02	45.29 / 1.74	0.11
J0507.9+6737	H	0.07 / 1.46	16.90 / 0.06	-0.15 / 0.01	0.63 / 0.01	1.09 / 0.01	45.81 / 0.09	5.60	0.07
1ES 0502 + 675	0.416	0.18 / 3.08	25.33 / 0.08	0.59 / 0.01	0.73 / 0.01	0.78 / 0.03	45.66 / 0.11	45.36 / 1.37	0.75
J0509.4+0542	I	0.11 / 1.93	14.39 / 0.04	-0.19 / 0.01	1.00 / 0.01	1.70 / 0.01	45.48 / 0.06		0.06
TXS 0506 + 056	0.336	0.10 / 0.24	23.28 / 0.01	0.94 / 0.01	1.16 / 0.01	1.27 / 0.01	45.44 / 0.02	45.31 / 1.57	0.01
J0521.7+2112	H	0.08 / 2.07	15.35 / 0.07	-0.01 / 0.01	0.84 / 0.01	1.34 / 0.01	44.61 / 0.10		0.08
VER J0521 + 211	0.108	0.16 / 1.26	23.81 / 0.03	0.80 / 0.01	0.96 / 0.01	1.28 / 0.01	44.80 / 0.05	44.75 / 1.74	0.11
J0550.5-3216	H	0.05 / 1.61	17.57 / 0.10	0.18 / 0.01	0.69 / 0.01	0.99 / 0.01	44.12 / 0.15		0.13
PKS 0548 - 322	0.069	0.25 / 2.16	25.12 / 0.04	0.66 / 0.01	0.76 / 0.01	0.78 / 0.02	43.13 / 0.06	42.76 / 0.86	0.34
J0648.7+1516	H	0.07 / 1.81	16.71 / 0.08	-0.03 / 0.01	0.68 / 0.01	1.11 / 0.01	44.69 / 0.11		0.06
RX J0648.7 + 1516	0.179	0.50 / 2.31	24.86 / 0.02	0.65 / 0.01	0.78 / 0.01	0.82 / 0.02	44.88 / 0.03	44.41 / 1.21	0.46
J0650.7+2503	H	0.07 / 1.28	16.65 / 0.05	-0.05 / 0.01	0.68 / 0.01	1.12 / 0.01	44.91 / 0.08	3.20	0.04
1ES 0647 + 250	0.203	0.50 / 2.07	24.33 / 0.02	0.65 / 0.01	0.78 / 0.01	1.36 / 0.02	45.11 / 0.03	44.86 / 1.45	0.28
J0710.4+5908	H	0.06 / 2.02	17.86 / 0.12	0.04 / 0.01	0.62 / 0.01	0.96 / 0.01	44.68 / 0.16	2.90	0.12
RGB J0710 + 591	0.125	0.14 / 0.91	24.86 / 0.03	0.59 / 0.01	0.69 / 0.01	0.95 / 0.01	43.86 / 0.04	43.67 / 1.07	0.10
J0721.9+7120	I	0.11 / 2.61	14.91 / 0.06	-0.31 / 0.01	0.88 / 0.01	1.59 / 0.02	45.33 / 0.09	2.10	0.26
S5 0716 + 714	0.127	0.09 / 0.85	23.03 / 0.04	0.82 / 0.01	1.04 / 0.01	1.30 / 0.01	45.07 / 0.06	45.03 / 2.00	0.06
J0739.2+0137	F	0.10 / 1.14	13.97 / 0.03	0.04 / 0.01	1.08 / 0.01	1.70 / 0.01	44.62 / 0.04	8.60	0.09
PKS 0736 + 017	0.189	0.16 / 0.99	21.69 / 0.03	1.03 / 0.01	1.22 / 0.01	1.93 / 0.01	45.34 / 0.04	44.40 / 1.57	0.06
J0809.8+5218	H	0.08 / 1.09	15.95 / 0.04	-0.09 / 0.01	0.75 / 0.01	1.25 / 0.01	44.59 / 0.06	3.30	0.02
1ES 0806 + 524	0.138	0.38 / 0.98	24.28 / 0.01	0.71 / 0.01	0.86 / 0.01	1.31 / 0.01	44.60 / 0.02	44.53 / 1.58	0.13
J0847.2+1134	H	0.06 / 2.08	17.46 / 0.10	-0.03 / 0.01	0.62 / 0.01	1.00 / 0.01	44.56 / 0.14		0.06
RBS 0723	0.198	0.56 / 5.93	25.09 / 0.05	0.59 / 0.01	0.71 / 0.01	0.55 / 0.05	44.35 / 0.07	43.94 / 0.91	1.95
J0854.8+2006	L	0.18 / 1.38	13.29 / 0.02	-0.46 / 0.01	1.39 / 0.01	2.47 / 0.01	45.80 / 0.03	8.80	0.04
OJ 287	0.306	0.07 / 0.82	21.55 / 0.04	1.30 / 0.01	1.63 / 0.01	1.45 / 0.01	45.54 / 0.06	45.08 / 1.64	0.05
J0958.7+6534	L	0.16 / 2.61	12.98 / 0.04	-0.21 / 0.01	1.45 / 0.01	2.42 / 0.01	45.18 / 0.05	5.00	0.08
S4 0954 + 65	0.367	0.07 / 1.00	21.57 / 0.05	1.37 / 0.01	1.66 / 0.01	1.45 / 0.01	45.40 / 0.08	45.02 / 1.57	0.09
J1010.2-3119	H	0.06 / 2.57	17.18 / 0.13	0.07 / 0.01	0.68 / 0.01	1.04 / 0.02	44.37 / 0.19	2.80	0.10
1RXS J101015.9 - 311909	0.143	0.25 / 1.81	24.18 / 0.03	0.65 / 0.01	0.76 / 0.01	1.25 / 0.02	44.38 / 0.05	43.85 / 0.99	0.31
J1015.0+4926	H	0.07 / 1.47	15.99 / 0.06	0.01 / 0.01	0.77 / 0.01	1.21 / 0.01	45.07 / 0.08	3.00	0.04
1ES 1011 + 496	0.212	0.13 / 0.72	24.55 / 0.03	0.73 / 0.01	0.87 / 0.01	1.04 / 0.01	45.21 / 0.04	45.27 / 1.75	0.05
J1103.6-2329	H	0.07 / 2.04	16.66 / 0.09	0.02 / 0.01	0.70 / 0.01	1.11 / 0.01	45.28 / 0.13		0.24
1ES 1101 - 232	0.186	0.32 / 0.95	24.93 / 0.01	0.67 / 0.01	0.79 / 0.01	0.84 / 0.01	44.57 / 0.02	43.91 / 0.88	0.14
J1104.4+3812	H	0.07 / 0.98	17.01 / 0.05	-0.05 / 0.01	0.65 / 0.01	1.06 / 0.01	44.26 / 0.06	0.50	0.13
Mkr 421	0.030	0.12 / 0.42	25.23 / 0.02	0.61 / 0.01	0.74 / 0.01	0.88 / 0.01	44.31 / 0.02	44.22 / 2.03	0.15
J1136.4+6736	H	0.06 / 2.08	17.49 / 0.11	0.04 / 0.01	0.64 / 0.01	1.00 / 0.01	44.39 / 0.16	2.60	0.12
RX J1136.5 + 6737	0.136	0.40 / 3.31	24.21 / 0.04	0.61 / 0.01	0.72 / 0.01	1.38 / 0.03	43.86 / 0.05	43.70 / 1.11	0.65
J1136.4+7009	H	0.06 / 1.78	16.35 / 0.08	0.08 / 0.01	0.75 / 0.01	1.15 / 0.01	43.56 / 0.11	0.80	0.10
Mkr 180	0.045	0.11 / 0.53	24.60 / 0.02	0.72 / 0.01	0.84 / 0.01	1.02 / 0.01	43.08 / 0.03	43.02 / 1.33	0.02

Table 1. Sample Data and Fitting Results

4FGL Name	class	$\beta_{\text{syn}}/(\sigma \times 10^{-4})$	$\log L_{\text{peak}}^{\text{syn}}/\sigma$	$\alpha_r/\sigma$	$\alpha_o/\sigma$	$\alpha_x/\sigma$	$\log L_{\text{peak}}^{\text{syn}}/\sigma$	$D_r$	$\chi_{\text{syn}}^2$
Other Name	z	$\beta_{\text{ic}}/(\sigma \times 10^{-4})$	$\log L_{\text{peak}}^{\text{ic}}/\sigma$	$\alpha_{\text{ir}}/\sigma$	$\alpha_{\text{uv}}/\sigma$	$\alpha_{\gamma}/\sigma$	$\log L_{\text{peak}}^{\text{ic}}/\sigma$	$\log L_{\gamma}/\sigma$	$\chi_{\text{ic}}^2$
(1)	(2)	(3)	(4)	(5)	(6)	(7)	(8)	(9)	(10)
J1159.5+2914	F	0.18 / 3.00	13.05 / 0.04	-0.39 / 0.01	1.48 / 0.02	2.58 / 0.02	46.08 / 0.06	6.40	0.14
TON 0599	0.729	0.09 / 0.78	21.89 / 0.04	1.39 / 0.01	1.72 / 0.02	1.48 / 0.01	46.57 / 0.05	45.96 / 1.70	0.05
J1217.9+3007	I	0.09 / 2.03	14.89 / 0.06	-0.01 / 0.01	0.91 / 0.01	1.46 / 0.01	44.39 / 0.09	0.40	0.11
1ES 1215 + 303	0.130	0.16 / 0.78	23.72 / 0.02	0.87 / 0.01	1.03 / 0.01	1.30 / 0.01	44.67 / 0.03	44.74 / 1.70	0.05
J1221.3+3010	H	0.06 / 1.56	17.21 / 0.07	-0.03 / 0.01	0.64 / 0.01	1.03 / 0.01	45.13 / 0.11	2.60	0.12
1ES 1218 + 304	0.184	0.32 / 0.62	24.61 / 0.01	0.61 / 0.01	0.73 / 0.01	1.05 / 0.01	45.10 / 0.01	44.78 / 1.43	0.07
J1221.5+2814	H	0.08 / 2.03	15.36 / 0.08	0.07 / 0.01	0.85 / 0.01	1.32 / 0.01	44.51 / 0.11	0.20	0.18
W Comae	0.102	0.18 / 1.32	23.77 / 0.03	0.82 / 0.01	0.96 / 0.01	1.33 / 0.01	44.45 / 0.05	43.93 / 1.53	0.14
J1224.4+2436	H	0.09 / 1.36	15.68 / 0.04	-0.12 / 0.01	0.78 / 0.01	1.31 / 0.01	44.19 / 0.06	3.00	0.01
MS 1221.8 + 2452	0.219	0.71 / 3.25	24.56 / 0.02	0.73 / 0.01	0.90 / 0.01	1.17 / 0.03	45.06 / 0.03	44.45 / 1.29	0.68
J1224.9+2122	F	0.13 / 5.92	13.87 / 0.11	-0.23 / 0.02	1.13 / 0.03	1.94 / 0.03	45.89 / 0.15	6.02	0.27
4C + 21.35	0.434	0.10 / 1.65	21.99 / 0.07	1.07 / 0.02	1.31 / 0.03	1.51 / 0.01	46.54 / 0.10	45.82 / 1.92	0.28
J1230.2+2517	I	0.12 / 2.88	14.61 / 0.06	-0.33 / 0.01	0.94 / 0.01	1.70 / 0.02	44.73 / 0.08	3.60	0.05
S3 1227 + 25	0.135	0.14 / 1.47	23.24 / 0.05	0.88 / 0.01	1.11 / 0.01	1.40 / 0.01	44.21 / 0.06	44.29 / 1.52	0.12
J1256.1-0547	F	0.13 / 2.25	12.84 / 0.04	0.01 / 0.01	1.42 / 0.01	2.25 / 0.01	46.60 / 0.05	18.00	0.28
3C 279	0.536	0.12 / 1.13	21.71 / 0.04	1.35 / 0.01	1.60 / 0.01	1.72 / 0.01	46.94 / 0.05	46.11 / 1.93	0.27
J1315.0-4236	H	0.07 / 3.13	16.99 / 0.13	-0.13 / 0.01	0.63 / 0.02	1.07 / 0.02	43.99 / 0.19	3.00	0.19
1ES 1312 - 423	0.105	0.21 / 4.14	24.85 / 0.09	0.59 / 0.01	0.73 / 0.02	0.93 / 0.04	43.36 / 0.13	43.32 / 0.79	1.48
J1427.0+2348	H	0.09 / 2.37	15.47 / 0.07	-0.10 / 0.01	0.81 / 0.01	1.35 / 0.01	46.20 / 0.10	2.70	0.11
PKS 1424 + 240	0.604	0.48 / 0.67	24.10 / 0.01	0.77 / 0.01	0.93 / 0.01	1.56 / 0.01	46.59 / 0.01	46.39 / 1.78	0.08
J1428.5+4240	H	0.08 / 1.73	17.18 / 0.07	-0.24 / 0.01	0.57 / 0.01	1.05 / 0.01	44.78 / 0.10	1.60	0.13
H 1426 + 428	0.129	0.65 / 2.97	24.56 / 0.02	0.53 / 0.01	0.68 / 0.01	1.17 / 0.03	44.52 / 0.03	43.79 / 1.09	0.55
J1442.7+1200	H	0.08 / 2.27	16.24 / 0.09	-0.09 / 0.01	0.71 / 0.01	1.19 / 0.01	44.47 / 0.12	2.10	0.08
1ES 1440 + 122	0.163	0.17 / 1.24	24.70 / 0.03	0.68 / 0.01	0.82 / 0.01	0.99 / 0.01	43.91 / 0.05	43.81 / 1.00	0.09
J1443.9+2501	F	0.10 / 3.22	13.39 / 0.08	0.19 / 0.01	1.19 / 0.02	1.79 / 0.02	44.77 / 0.12		0.08
PKS 1441 + 25	0.939	0.09 / 1.64	22.51 / 0.08	1.14 / 0.01	1.33 / 0.02	1.37 / 0.01	46.21 / 0.11	46.27 / 1.58	0.16
J1443.9-3908	H	0.09 / 1.64	15.82 / 0.05	-0.16 / 0.01	0.75 / 0.01	1.29 / 0.01	44.04 / 0.07	3.00	0.06
PKS 1440 - 389	0.065	0.36 / 3.43	24.31 / 0.04	0.71 / 0.01	0.87 / 0.01	1.27 / 0.03	43.94 / 0.06	43.88 / 1.50	0.78
J1512.8-0906	F	0.11 / 1.24	13.67 / 0.03	-0.03 / 0.01	1.16 / 0.01	1.87 / 0.01	45.50 / 0.04	14.50	0.02
PKS 1510 - 089	0.360	0.12 / 0.89	21.72 / 0.03	1.11 / 0.01	1.32 / 0.01	1.72 / 0.01	46.76 / 0.04	45.89 / 2.03	0.06
J1517.7-2422	L	0.12 / 0.86	13.95 / 0.02	-0.11 / 0.01	1.10 / 0.01	1.82 / 0.01	43.86 / 0.03		0.01
AP Lib	0.048	0.05 / 0.58	22.08 / 0.05	1.04 / 0.01	1.26 / 0.01	1.26 / 0.01	43.75 / 0.07	43.55 / 1.62	0.03
J1555.7+1111	H	0.09 / 0.84	15.78 / 0.03	-0.20 / 0.01	0.75 / 0.01	1.31 / 0.01	46.04 / 0.04	5.10	0.04
PG 1553 + 113	0.360	0.61 / 1.23	24.71 / 0.01	0.70 / 0.01	0.87 / 0.01	0.98 / 0.01	46.30 / 0.01	46.07 / 1.80	0.26
J1653.8+3945	H	0.06 / 1.43	16.30 / 0.07	0.09 / 0.01	0.76 / 0.01	1.15 / 0.01	44.04 / 0.09	1.50	0.16
Mkr 501	0.033	0.13 / 0.85	25.17 / 0.03	0.72 / 0.01	0.84 / 0.01	0.88 / 0.01	44.03 / 0.04	43.82 / 1.80	0.21
J1725.0+1152	H	0.07 / 2.41	16.46 / 0.10	-0.01 / 0.01	0.71 / 0.01	1.14 / 0.02	44.92 / 0.14	1.10	0.10
H 1722 + 119	0.180	0.18 / 0.78	24.36 / 0.02	0.68 / 0.01	0.81 / 0.01	1.11 / 0.01	44.77 / 0.03	44.73 / 1.46	0.04
J1728.3+5013	H	0.07 / 1.13	16.37 / 0.05	0.06 / 0.01	0.74 / 0.01	1.15 / 0.01	43.60 / 0.07	0.01	0.02
1ES 1727 + 502	0.055	0.06 / 1.23	25.66 / 0.09	0.71 / 0.01	0.83 / 0.01	0.88 / 0.01	43.46 / 0.13	43.41 / 1.40	0.10
J1744.0+1935	H	0.06 / 1.32	16.57 / 0.07	0.18 / 0.01	0.76 / 0.01	1.10 / 0.01	43.77 / 0.10		0.06
1ES 1741 + 196	0.084	0.90 / 3.11	24.35 / 0.02	0.73 / 0.01	0.84 / 0.01	1.61 / 0.03	43.92 / 0.02	43.33 / 1.12	0.56
J1751.5+0938	L	0.17 / 2.08	13.23 / 0.03	-0.37 / 0.01	1.39 / 0.01	2.43 / 0.01	45.44 / 0.04	11.90	0.08
OT 081	0.322	0.07 / 0.67	21.21 / 0.04	1.30 / 0.01	1.62 / 0.01	1.47 / 0.01	45.67 / 0.06	45.01 / 1.54	0.03
J2000.0+6508	H	0.07 / 1.44	16.82 / 0.07	-0.01 / 0.01	0.68 / 0.01	1.09 / 0.01	44.20 / 0.09	5.20	0.10
1ES 1959 + 650	0.047	0.13 / 1.29	24.72 / 0.05	0.65 / 0.01	0.77 / 0.01	0.99 / 0.01	44.05 / 0.07	43.92 / 1.74	0.66
J2009.4-4849	H	0.07 / 1.18	16.48 / 0.05	0.03 / 0.01	0.72 / 0.01	1.13 / 0.01	44.78 / 0.07		0.09
PKS 2005 - 489	0.071	0.19 / 0.67	24.42 / 0.02	0.69 / 0.01	0.82 / 0.01	1.10 / 0.01	43.84 / 0.02	43.80 / 1.48	0.07
J2039.5+5218	H	0.07 / 2.59	16.20 / 0.11	-0.02 / 0.01	0.74 / 0.01	1.18 / 0.02	43.17 / 0.15	3.60	0.08
1ES 2037 + 521	0.053	0.42 / 4.71	24.67 / 0.05	0.70 / 0.01	0.84 / 0.01	1.02 / 0.04	42.71 / 0.07	42.74 / 0.82	1.10
J2158.8-3013	H	0.10 / 1.31	15.92 / 0.04	-0.40 / 0.01	0.68 / 0.01	1.32 / 0.01	45.50 / 0.05		0.09
PKS 2155 - 304	0.116	0.23 / 0.84	24.54 / 0.02	0.63 / 0.01	0.83 / 0.01	1.07 / 0.01	45.46 / 0.02	45.08 / 1.88	0.38
J2202.7+4216	L	0.20 / 2.42	12.95 / 0.03	-0.55 / 0.01	1.58 / 0.01	2.85 / 0.01	44.51 / 0.04	4.40	0.10
BL Lacertae	0.069	0.05 / 1.29	21.28 / 0.09	1.48 / 0.01	1.87 / 0.01	1.36 / 0.01	44.62 / 0.13	44.26 / 1.89	0.21
J2250.0+3825	H	0.07 / 2.41	16.33 / 0.11	0.05 / 0.01	0.74 / 0.01	1.15 / 0.01	44.18 / 0.15	2.00	0.10
B3 2247 + 381	0.119	0.20 / 1.67	24.77 / 0.04	0.71 / 0.01	0.84 / 0.01	0.97 / 0.02	44.04 / 0.05	43.75 / 1.05	0.24
J2324.7-4041	H	0.10 / 1.21	15.79 / 0.04	-0.26 / 0.01	0.73 / 0.01	1.32 / 0.01	44.81 / 0.05		0.02
1ES 2322 - 409	0.174	0.17 / 1.42	23.87 / 0.04	0.69 / 0.01	0.87 / 0.01	1.27 / 0.01	44.33 / 0.05	44.21 / 1.14	0.13
J2347.0+5141	H	0.06 / 0.97	16.72 / 0.05	0.03 / 0.01	0.70 / 0.01	1.10 / 0.01	43.66 / 0.07	3.60	0.04
1ES 2344 + 514	0.044	0.24 / 2.00	24.95 / 0.04	0.67 / 0.01	0.79 / 0.01	0.87 / 0.02	43.88 / 0.06	43.40 / 1.44	0.57
J2359.0-3038	H	0.07 / 1.09	17.18 / 0.05	-0.06 / 0.01	0.63 / 0.01	1.04 / 0.01	44.80 / 0.07	2.90	0.07
H 2356 - 309	0.165	0.32 / 0.94	24.38 / 0.01	0.60 / 0.01	0.72 / 0.01	1.20 / 0.01	44.53 / 0.02	43.75 / 1.03	0.18
J0733.4+5152	B	0.07 / 1.47	16.88 / 0.06	-0.12 / 0.01	0.64 / 0.01	1.09 / 0.01	43.65 / 0.09		0.04
PGC 2402248	0.065	0.40 / 4.44	24.44 / 0.05	0.60 / 0.01	0.74 / 0.01	1.20 / 0.04	43.14 / 0.07	42.68 / 0.81	0.99



**Table 2.** Jet Radiation Zone Parameters

TeV Source Name	$\log D_{\text{Th}}$	$\log D_{\text{KN}}$	$\log B$	$\log R$	$\log \gamma_{\text{p}}$
(1)	(2)	(3)	(4)	(5)	(6)
SHBL J001355.9 – 185406	-0.80	0.98	-2.45	16.89	4.70
RGB J0152 + 017	-0.18	1.16	-3.34	17.15	4.88
1ES 0229 + 200	-1.02	1.39	-4.61	17.50	5.62
1RXS J023832.6 – 311658	-0.65	1.20	-2.47	17.22	4.59
RBS 0413	0.12	1.24	-3.91	17.28	5.35
1ES 0347 – 121	-1.09	1.14	-3.83	17.12	5.69
1ES 0414 + 009	-0.63	1.19	-2.86	17.20	4.93
1ES 0502 + 675	-0.12	1.37	-3.75	17.47	5.37
PKS 0548 – 322	-0.86	1.76	-4.91	18.06	5.33
RGB J0710 + 591	-1.12	1.30	-3.71	17.36	5.35
RBS 0723	-0.87	1.18	-3.91	17.18	5.52
1RXS J101015.9 – 311909	-1.08	1.09	-2.87	17.05	4.79
1ES 1101 – 232	-0.04	1.62	-3.62	17.84	4.83
RX J1136.5 + 6737	-1.20	1.05	-2.67	16.98	4.86
Mkr 180	-0.28	1.37	-3.57	17.47	4.72
1ES 1218 + 304	-0.78	1.13	-3.01	17.10	5.02
W Comae	0.27	1.36	-2.00	17.46	3.69
MS 1221.8 + 2452	0.06	1.03	-2.97	16.96	4.69
1ES 1312 – 423	-0.59	1.00	-3.12	16.91	5.19
H 1426 + 428	-0.78	0.75	-2.24	16.54	5.07
1ES 1440 + 122	0.02	1.26	-2.97	17.31	4.71
1ES 1727 + 502	0.07	1.64	-5.32	17.87	5.50
1ES 1741 + 196	-0.67	1.45	-3.79	17.59	4.66
PKS 2005 – 489	-0.13	1.46	-2.81	17.61	4.41
B3 2247 + 381	-0.16	1.42	-3.71	17.55	4.82
H 2356 – 309	-0.86	0.99	-2.53	16.90	4.88
TXS 0210 + 515	-0.62	1.39	-3.52	17.49	4.57
RX J0648.7 + 1516	-0.40	1.23	-3.55	17.26	5.08
1ES 2037 + 521	-0.22	1.16	-3.36	17.16	4.82
KUV 00311 – 1938	0.39	1.16	-2.21	17.15	4.54
PKS 0301 – 243	0.46	1.75	-2.96	18.04	3.89
PKS 0447 – 439	0.38	1.17	-1.89	17.16	4.11
1ES 0647 + 250	-0.53	1.06	-2.56	17.01	4.69
1ES 0806 + 524	0.01	1.13	-2.35	17.10	4.37
1ES 1011 + 496	0.13	1.45	-3.11	17.58	4.48
Mkr 421	-0.52	1.18	-4.06	17.19	5.46
PKS 1424 + 240	0.48	1.38	-1.97	17.48	3.99
PKS 1440 – 389	0.05	1.00	-2.25	16.91	4.40
PG 1553 + 113	0.51	1.35	-2.63	17.45	4.50
Mkr 501	-0.02	1.60	-4.55	17.82	5.06
H 1722 + 119	-0.29	1.26	-2.70	17.30	4.54
1ES 1959 + 650	-0.55	1.16	-3.35	17.16	5.00
PKS 2155 – 304	0.34	1.01	-1.90	16.93	4.46
1ES 2322 – 409	0.11	0.92	-1.12	16.80	3.98
VER J0521 + 211	0.27	1.23	-1.85	17.26	3.77
1ES 2344 + 514	-0.56	1.20	-4.06	17.22	5.24
S2 0109 + 22	1.06	1.18	-0.76	17.18	3.22
3C 66A	0.76	1.48	-1.24	17.63	3.13
TXS 0506 + 056	1.01	1.23	-0.42	17.26	2.97
S5 0716 + 714	0.56	0.89	0.36	16.75	2.98
1ES 1215 + 303	0.54	1.24	-1.72	17.28	3.58
S3 1227 + 25	0.81	0.98	-0.05	16.88	3.05
OJ 287	1.33	0.86	2.84	16.70	1.29
S4 0954 + 65	1.36	0.93	2.28	16.81	1.32
AP Lib	0.64	0.77	1.26	16.56	2.11
OT 081	1.07	0.67	3.17	16.42	1.16
BL Lacertae	1.23	0.55	3.14	16.25	1.16
S3 0218 + 35	2.12	1.21	0.66	17.23	2.07
PKS 0736 + 017	0.41	0.80	1.51	16.62	1.87
TON 0599	1.50	1.01	1.98	16.92	1.59
4C + 21.35	0.84	0.86	1.71	16.70	1.97
3C 279	1.75	1.42	1.85	17.54	1.13
PKS 1441 + 25	0.97	1.33	-0.57	17.41	2.42
PKS 1510 – 089	0.70	0.85	1.63	16.69	1.79
PGC 2402248	-0.74	0.82	-2.52	16.65	4.93

Note. Column (2) gives the physical parameters of the Doppler factor ( $\log D_{\text{Th}}$ ) obtained from the Thomson scattering region; Columns (3)-(6) give the physical parameters obtained from the KN scattering region — namely, the Doppler factor ( $\log D_{\text{KN}}$ ), magnetic field strength ( $\log B$ ), radiative zone radius ( $\log R$ ), and peak Lorentz factor ( $\log \gamma_{\text{p}}$ ).

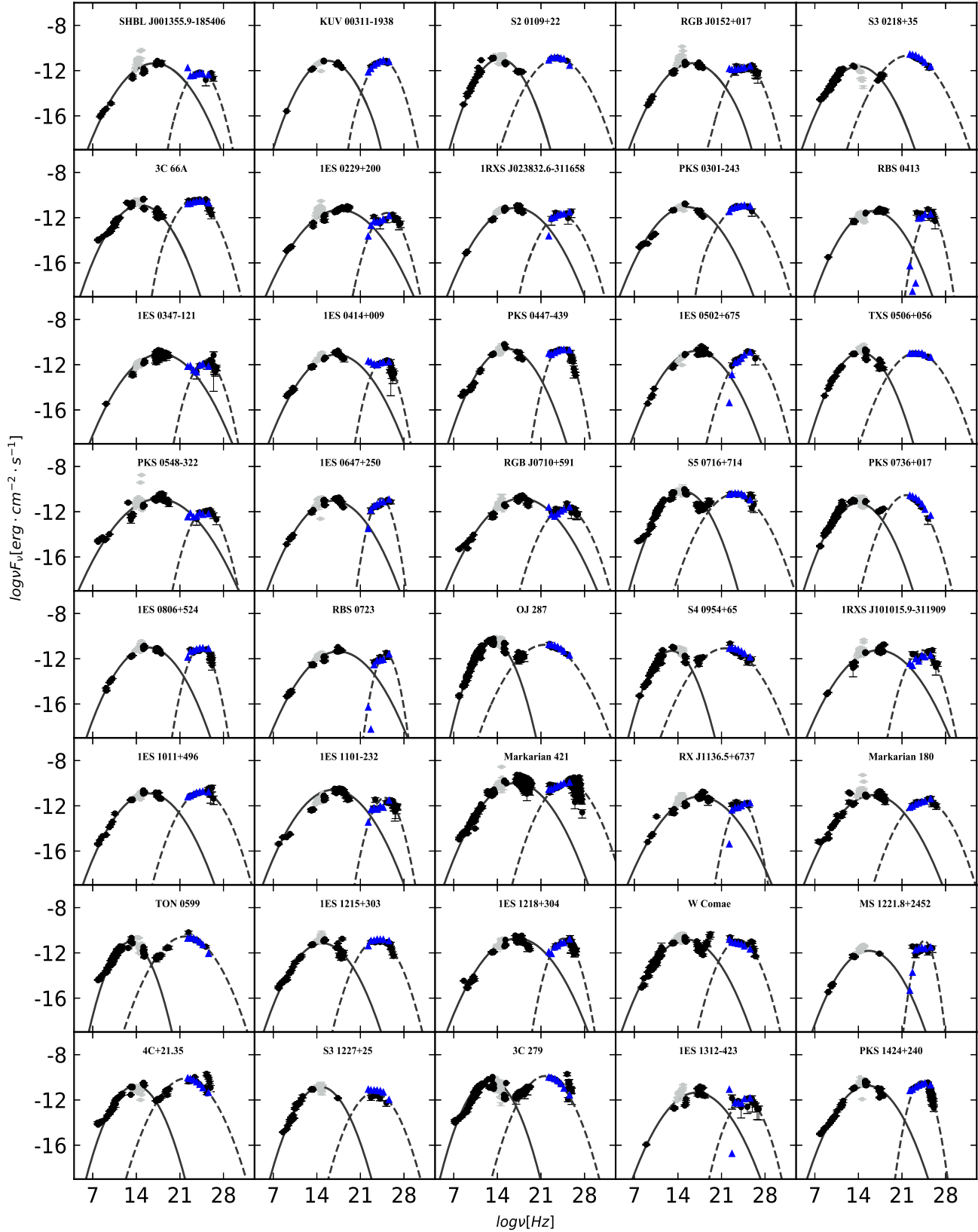


**Figure 1.** The SEDs of Fermi TeV blazars. The dots represent the data from the SSDC, and the square points represent the data of the thermal radiation bump. The triangles represent the data from the 4FGL (Abdollahi et al. 2020). The solid line is the fitting line in the synchrotron region, and the dashed line is the fitting line in the ICs region.

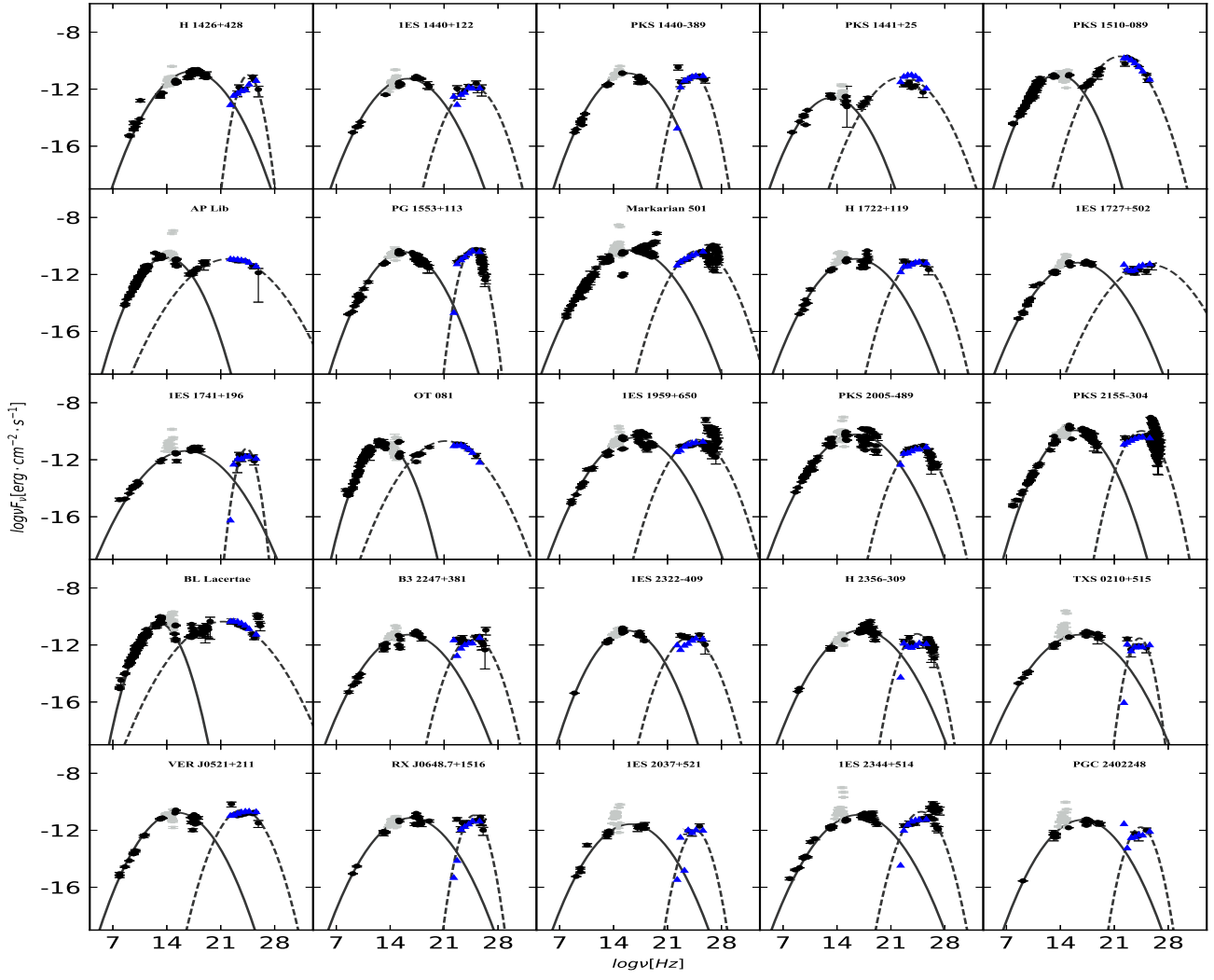


Figure 2. The SEDs of the remaining Fermi TeV blazars.

**Table 3.** Statistical Values for the Fitting Results

Parameters	Items	HBLs	IBLs	LBLs	FSRQs	All
(1)	(2)	(3)	(4)	(5)	(6)	(7)
$\beta_{\text{syn}}$	Mean	0.07	0.11	0.16	0.12	0.09
	Max	0.10	0.12	0.20	0.18	0.20
	Min	0.05	0.09	0.12	0.09	0.05
$\beta_{\text{ic}}$	Mean	0.31	0.12	0.06	0.11	0.25
	Max	0.90	0.16	0.07	0.16	0.90
	Min	0.06	0.09	0.05	0.08	0.05
$\log \nu_{\text{peak}}^{\text{syn}}$	Mean	16.53	14.64	13.28	13.54	15.77
	Max	17.94	14.91	13.95	13.98	17.94
	Min	15.35	14.39	12.95	12.84	12.84
$\log \nu_{\text{peak}}^{\text{ic}}$	Mean	24.61	23.37	21.54	21.92	23.96
	Max	25.66	23.72	22.08	22.51	25.66
	Min	23.77	23.03	21.21	21.69	21.21
$\alpha_{\text{r}}$	Mean	-0.04	-0.18	-0.34	-0.04	-0.08
	Max	0.18	0.05	-0.11	0.19	0.19
	Min	-0.40	-0.33	-0.55	-0.39	-0.55
$\alpha_{\text{ir}}$	Mean	0.67	0.89	1.30	1.16	0.79
	Max	0.83	0.94	1.48	1.39	1.48
	Min	0.53	0.82	1.04	1.03	0.53
$\alpha_{\text{o}}$	Mean	0.71	0.95	1.38	1.22	0.84
	Max	0.86	1.00	1.58	1.48	1.58
	Min	0.57	0.88	1.10	1.07	0.57
$\alpha_{\text{uv}}$	Mean	0.81	1.10	1.61	1.39	0.96
	Max	0.96	1.16	1.87	1.72	1.87
	Min	0.66	1.03	1.26	1.20	0.66
$\alpha_{\text{x}}$	Mean	1.15	1.61	2.40	1.96	1.38
	Max	1.35	1.74	2.85	2.58	2.85
	Min	0.95	1.46	1.82	1.62	0.95
$\alpha_{\gamma}$	Mean	1.06	1.32	1.40	1.60	1.17
	Max	1.61	1.41	1.47	1.93	1.93
	Min	0.32	1.22	1.26	1.37	0.32
$\log L_{\text{peak}}^{\text{syn}}$	Mean	44.58	45.15	44.96	45.60	44.77
	Max	46.20	45.77	45.80	46.60	46.60
	Min	43.17	44.39	43.86	44.62	43.17
$\log L_{\text{peak}}^{\text{ic}}$	Mean	44.39	45.15	45.00	46.44	44.73
	Max	46.59	46.24	45.67	46.94	46.94
	Min	42.71	44.21	43.75	45.34	42.71

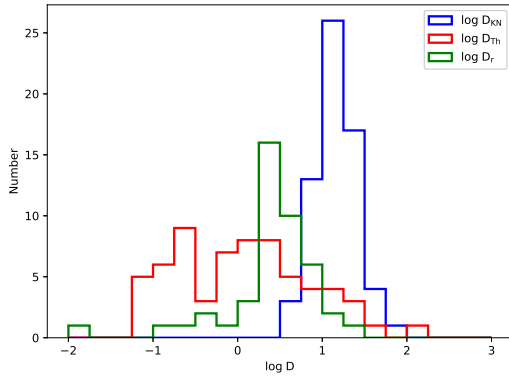
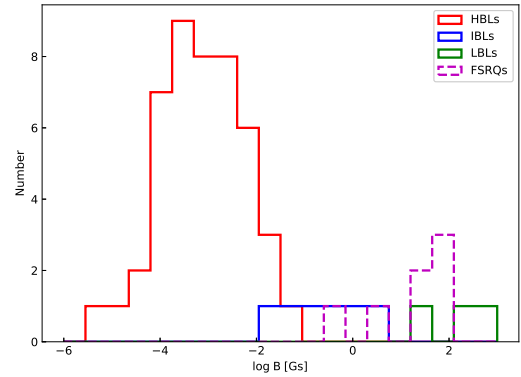
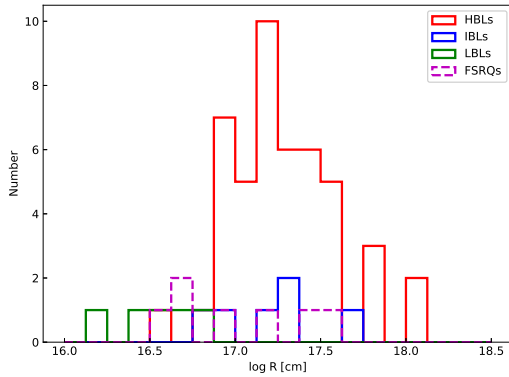
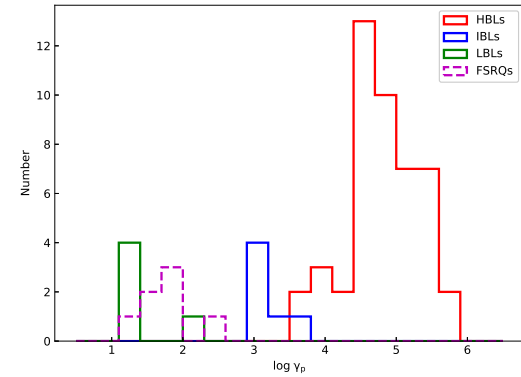
Note. Column (1) gives the parameter, where  $\log \nu_{\text{peak}}^{\text{syn}}$  and  $\log \nu_{\text{peak}}^{\text{ic}}$  in units of hertz,  $\log L_{\text{peak}}^{\text{syn}}$  and  $\log L_{\text{peak}}^{\text{ic}}$  are in units of ergs per second; Column (2) indicates the mean value (Mean), maximum value (Max), and minimum value (Min) of the parameter items.

$\langle \alpha_{\text{uv}} \rangle_{\text{BLLacs}} = 1.17$ , and  $\langle \alpha_{\text{x}} \rangle_{\text{BLLacs}} = 1.72$ . These values are close to the results of Fan et al. (2017) and Cheng et al. (2000). The mean curvatures of the synchrotron bump and ICs bump in the peak satisfy the following relations:  $\langle \beta_{\text{ic}} \rangle = 2.87 \langle \beta_{\text{syn}} \rangle$ , and  $\langle \beta_{\text{ic}} \rangle_{\text{HBLs}} = 4.35 \langle \beta_{\text{syn}} \rangle_{\text{HBLs}}$ . The latter of the above results is more similar to that of Massaro et al. (2004a,b), indicating that the curvature relation of TeV HBLs conforms to the condition of the KN scattering region. (2) There are many ways to estimate the Doppler factor at present. In our model, when we derive the Doppler factor, we assume that  $D \approx \Gamma$ , which requires that the Doppler factor be greater than 1. Therefore, it can be seen from the Doppler factor histogram that KN scattering region calculation is more suitable. Therefore, Equation (17) is used to calculate the parameters of the jet radiation zone. Within the sample, the Doppler factor is in the range of  $3.58 \leq D \leq 57.65$ . The median values of  $D$  of the HBLs, IBLs, LBLs, FSRQs, and total TeV blazars are 15.98, 16.09, 5.83, 10.12, and 15.19, respectively. This result is consistent with that of Chen (2018), which is within a reasonable range of  $1 \leq D \leq 100$ . The magnetic field strength is in the range of  $4.82 \times 10^{-6} \text{ G} \leq B \leq 1.47 \times 10^3 \text{ G}$ . The median values of  $B$  of the HBLs, IBLs, LBLs, FSRQs, and total TeV blazars are  $1.03 \times 10^{-3}$ , 0.26,  $6.96 \times 10^2$ , 42.88 and 0.003 G, respectively. Zhang et al. (2012) estimated the magnetic field strength of GeV-TeV BL Lac objects, and gave a

**Table 4.** Results of Correlation Text and Linear Regression Analysis

$y \sim x$	$a \sim \sigma_a$	$b \sim \sigma_b$	$r'$	$r$	$N$	$\rho$	$P$
(1)	(2)	(3)	(4)	(5)	(6)	(7)	(8)
$\log \nu_{\text{peak}}^{\text{ic}} \sim \log \nu_{\text{peak}}^{\text{syn}}$	$12.80 \pm 0.70$	$0.70 \pm 0.04$	0.79	0.82	64	0.79	$< 10^{-4}$
$\log L'_{\text{peak}} \sim \log L'_{\gamma}$	$3.60 \pm 1.30$	$0.95 \pm 0.03$	0.93	0.93	64	0.95	$< 10^{-4}$
$\alpha_r \sim \log \nu_{\text{peak}}^{\text{syn}}$	$-0.60 \pm 0.20$	$0.04 \pm 0.02$	0.07	0.17	64	0.22	$> 0.05$
$\alpha_{\text{ir}} \sim \log \nu_{\text{peak}}^{\text{syn}}$	$3.10 \pm 0.13$	$-0.16 \pm 0.01$	0.83	0.89	64	-0.96	$< 10^{-4}$
$\alpha_o \sim \log \nu_{\text{peak}}^{\text{syn}}$	$3.30 \pm 0.10$	$-0.17 \pm 0.01$	0.83	0.89	64	-0.97	$< 10^{-4}$
$\alpha_{\text{uv}} \sim \log \nu_{\text{peak}}^{\text{syn}}$	$3.80 \pm 0.20$	$-0.20 \pm 0.01$	0.81	0.89	64	-0.98	$< 10^{-4}$
$\alpha_x \sim \log \nu_{\text{peak}}^{\text{syn}}$	$5.60 \pm 0.30$	$-0.30 \pm 0.02$	0.76	0.87	64	-0.96	$< 10^{-4}$
$\alpha_{\gamma} \sim \log \nu_{\text{peak}}^{\text{ic}}$	$6.20 \pm 0.50$	$-0.22 \pm 0.02$	0.59	0.44	64	-0.86	$< 10^{-4}$
$1/\beta_{\text{syn}} \sim \log \nu_{\text{peak}}^{\text{syn}}$	$-19.20 \pm 2.90$	$2.20 \pm 0.20$	0.66	0.80	64	0.81	$< 10^{-4}$
$1/\beta_{\text{ic}} \sim \log \nu_{\text{peak}}^{\text{ic}}$	$70.80 \pm 9.00$	$-2.80 \pm 0.40$	0.44	0.42	64	-0.54	$< 10^{-4}$
$\log \nu_{\text{peak}}^{\text{ic}} \sim \log \gamma_p$	$19.80 \pm 0.10$	$0.76 \pm 0.02$	0.96	0.97	64	0.94	$< 10^{-4}$
$\log B \sim \log \gamma_p$	$3.60 \pm 0.80$	$-1.40 \pm 0.20$	0.60	-	46	-0.79	$< 10^{-4}$
$\log R \sim \log \gamma_p$	$17.20 \pm 0.50$	$0.01 \pm 0.10$	0.02	-	46	0.03	$> 0.05$

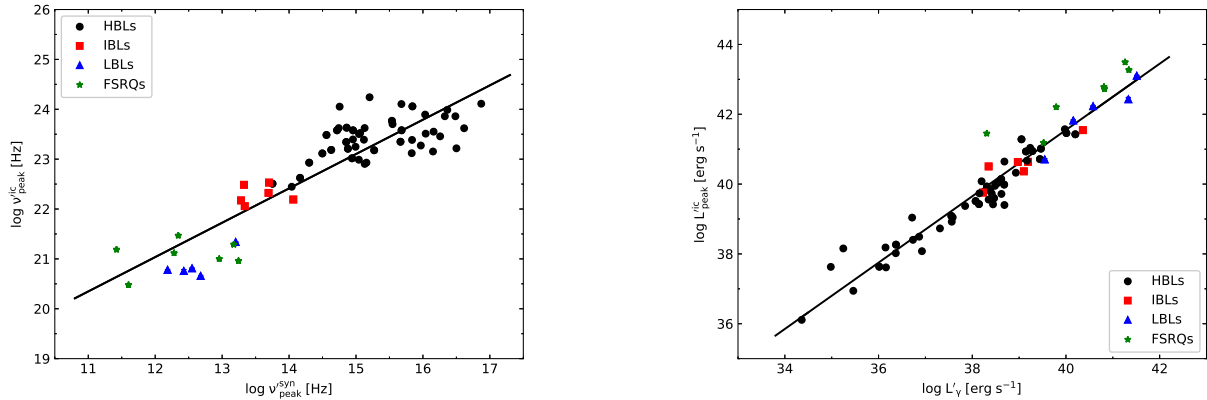
Note. Column (1) gives the relation  $y = a + bx$ ; Column (2) gives the intercept and the corresponding uncertainty; Column (3) gives the slope and the corresponding uncertainty; Column (4) gives the linear correlation coefficient in the co-moving frame; Column (5) gives the linear correlation coefficient in the observer's coordinate system; Column (6) gives the number of the sources; Column (7) gives the Spearman correlation coefficient; and Column (8) gives the chance probability.


**Figure 3.** The Doppler factor distributions for the TeV blazars.

**Figure 4.** Distribution of magnetic field strength for different types of TeV blazars.

**Figure 5.** Distribution of radiative zone radius for different types of TeV blazars.

**Figure 6.** Distribution of peak Lorentz factor for different types of TeV blazars.

typical value of  $0.1 \text{ G} \leq B \leq 0.6 \text{ G}$ . In our results, the magnetic field strengths of LBLs and FSRQs are overestimated. The radiative zone radius is in the range of  $1.76 \times 10^{16} \text{ cm} \leq R \leq 1.14 \times 10^{18} \text{ cm}$ . The median values of  $R$  of the HBLs, IBLs, LBLs, FSRQs, and total TeV blazars are  $1.66 \times 10^{17}$ ,  $1.67 \times 10^{17}$ ,  $3.65 \times 10^{16}$ ,  $8.34 \times 10^{16}$  and  $1.53 \times 10^{17} \text{ cm}$ , respectively. Our results are close to the result of Zhang et al. (2012), which is within the reasonable estimation range of  $10^{15} \text{ cm} \leq R \leq 10^{17} \text{ cm}$ . The peak Lorentz factor is in the range of  $13.57 \leq \gamma_p \leq 4.86 \times 10^5$ . The median values of  $\gamma_p$  of the HBLs, IBLs, LBLs, FSRQs, and total TeV blazars are  $6.34 \times 10^4$ ,  $1.23 \times 10^3$ ,  $19.36$ ,  $73.91$ , and  $3.58 \times 10^4$ , respectively. The range of the initial Lorentz factor  $\gamma_0$  is  $100 \leq \gamma_0 \leq 1000$  and the relationship between  $\gamma_p$  and  $\gamma_0$  is  $\gamma_p = \gamma_0 10^{-\frac{s}{2\tau}}$ . We can roughly give the reasonable range of the peak Lorentz factor as  $10^4 \leq \gamma_p \leq 10^5$  (Zhang et al. 2015; Ghisellini & Tavecchio 2015; Chen 2018). (3) Most of the TeV blazars are HBLs, so we can reasonably estimate their physical parameters based on the above results, as follows: for the HBL sources, the reasonable range of jet radiation zone parameters is  $5.6 \leq D \leq 31.6$ ,  $6.3 \times 10^{-5} \text{ G} \leq B \leq 1.1 \times 10^{-2} \text{ G}$ ,  $7.5 \times 10^{16} \text{ cm} \leq R \leq 4.2 \times 10^{17} \text{ cm}$ , and  $2.5 \times 10^4 \leq \gamma_p \leq 4.0 \times 10^5$ , as shown in Figures 3– 6.

#### 4.1. Intrinsic Synchrotron Peak Frequency versus Intrinsic ICs Peak Frequency

We now consider the relation between intrinsic synchrotron peak frequency and intrinsic ICs peak frequency. The results for our sample are shown in Figure 7 and described as follows: (1) Sources with high intrinsic synchrotron peak frequency have high intrinsic ICs peak frequency for TeV blazars. (2) According to the Spearman correlation test and linear regression analysis, there is a strong positive correlation between them and the empirical relation can be obtained by linear regression analysis. The results are listed in Table 4. (3) In the observer's coordinate system, we compare the relation  $\frac{\nu_{\text{peak}}^{\text{ic}}}{\nu_{\text{peak}}^{\text{syn}}} \simeq \frac{4}{3} (\gamma_{\text{peak}}^{\text{SSC}})^2$ ,  $\gamma_{\text{peak}}^{\text{SSC}} \leq 2 \times 10^4$  obtained here with that of Abdo et al. (2010) and find that the two are similar, the relative error being 6.2%. Considering that most of the sources in the sample are HBLs, this indicates that the radiation of TeV HBLs can well satisfy the SSC model.



**Figure 7.** The relation between intrinsic synchrotron peak frequency and intrinsic ICs peak frequency. **Figure 8.** The relation between intrinsic  $\gamma$ -ray luminosity and intrinsic ICs peak luminosity.

#### 4.2. Intrinsic $\gamma$ -Ray Luminosity versus Intrinsic ICs Peak Luminosity

At present, the range of peak luminosities of the ICs energy spectrum can usually be determined by performing an energy spectrum fitting. In the observations, the  $\gamma$ -ray photons of blazar radiation have a higher energy, and we consider whether there is a certain intrinsic connection between the two luminosities. The relation between intrinsic  $\gamma$ -ray luminosity at an energy of 20 GeV and ICs peak luminosity is shown in Figure 8. According to the results of the Spearman correlation test and linear regression analysis (Table 4), we draw the following conclusions: (1) There is a strong positive correlation between the luminosities, and their empirical relation can be obtained according to linear regression analysis, as shown in Table 4. The Spearman correlation coefficient is 0.95, and the slope is close to 1, indicating that the two luminosity values are very close to each other. (2) In the observer's coordinate system, we can get the following empirical formula:

$$\log L_{\text{peak}}^{\text{ic}} = (1.01 \pm 0.04) \log L_{\gamma} + (0.08 \pm 1.54) \quad (20)$$

where the Spearman test yields a correlation coefficient  $\rho = 0.96$  and the chance probability is  $P < 10^{-4}$ . (3) The observed quantity  $L_\gamma$ , which can be obtained using Equation (18), has a range of  $4.37 \times 10^{42} \text{ erg s}^{-1} \leq L_\gamma \leq 2.46 \times 10^{46} \text{ erg s}^{-1}$  in our sample; therefore, the ICs peak luminosity can be estimated within the range of  $8.66 \times 10^{42} \text{ erg s}^{-1} \leq L_{\text{peak}}^{\text{ic}} \leq 5.09 \times 10^{46} \text{ erg s}^{-1}$  according to Equation (20).

#### 4.3. Intrinsic Peak Frequency versus the Spectral Index

Figure 9 shows the relation between intrinsic peak frequency and the spectral index of each band in different types of TeV blazars. Since the peak frequency depends strongly on the Doppler factor (Nieppola et al. 2008), we use Doppler corrections and redshift corrections to study the intrinsic relation between peak frequency and the spectral index of each band. In order to clarify the correlation between  $\nu_{\text{peak}}$  and  $\alpha_\nu$ , the Spearman correlation test and a linear regression analysis have been conducted and the results are shown in Table 4. We get the following results: (1) There is not any correlation between the spectral indices and intrinsic synchrotron peak frequencies at radio bands. (2) The spectral indices depend strongly on the intrinsic synchrotron peak frequencies, i.e., the spectra of the source become hard when the intrinsic synchrotron peak frequencies increase in the infrared, optical, ultraviolet, and X-ray bands. (3) There is a strong negative correlation between intrinsic ICs peak frequency and the spectral index of  $\gamma$ -ray bands. It should be noted that their negative correlation is quite different from that of the synchrotron region, showing an inverse L-shaped reduction. (4) If radio bands are excluded, there is a negative correlation between the intrinsic peak frequency and the spectral index of each band. This indicates that the radio radiation generated by synchrotron radiation in the jet is optically thick, and the radio photons are emitted only when the depth of light decreases downstream of the jet. The infrared, optical, ultraviolet, and X-ray bands are all optically thin. This shows that the radiating region radius of the radio band is different from that of the other bands. There is radiation loss in each band, but the loss mechanism in the synchrotron radiation region is obviously different from that in the ICs region.

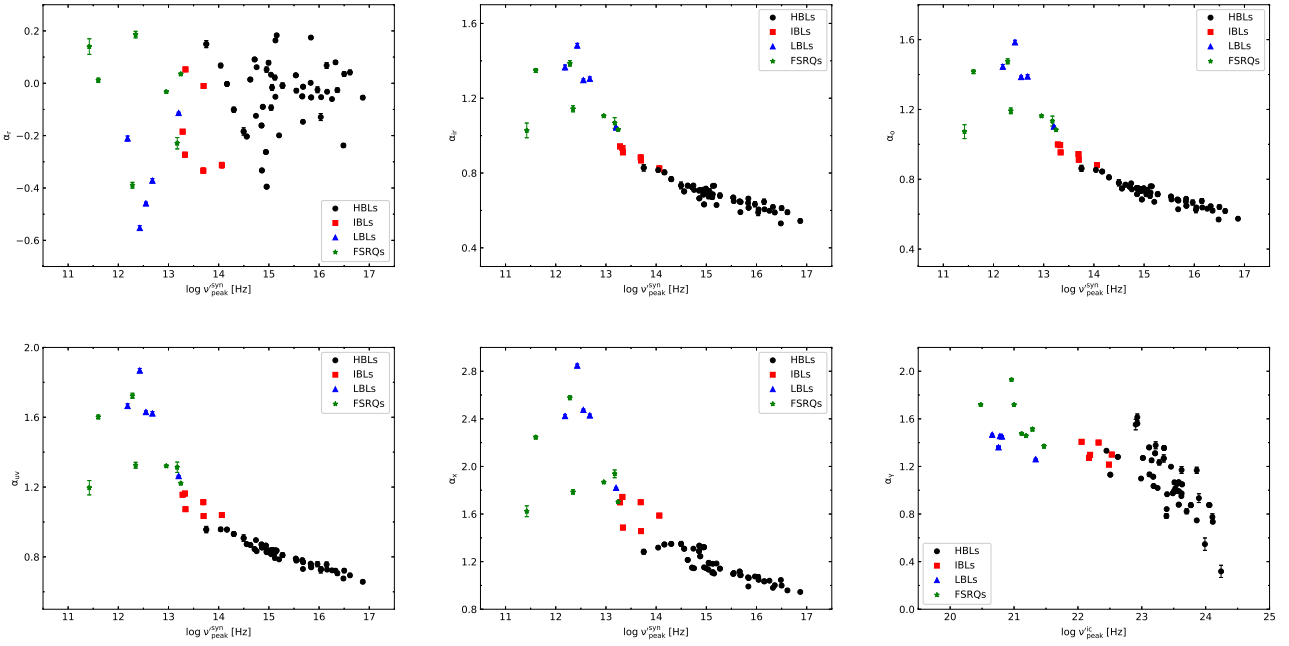


Figure 9. The relation between intrinsic peak frequency and the spectral index.

#### 4.4. Intrinsic Peak Frequency versus Curvature

As an important parameter of the energy spectrum, the curvatures of the synchrotron bump and ICs bump are essential for studying the particle acceleration mechanism. Equation (10) is used to define the energy spectrum curvature parameter  $\beta$  at the peak. In the process of stochastic acceleration, the decrease of curvature leads to the shift of peak energy toward higher energies. Chen (2014) studied the curvature of the blazars in depth and gave

three possible explanations for the acceleration mechanism according to the relation between the synchrotron peak frequency and the curvature of the synchrotron bump. From the result of our fit, we are able to investigate possible relations between the intrinsic peak frequency and the curvature of the energy spectrum at the peak. Based on the Spearman correlation test and linear regression analysis in Table 4, the following results can be obtained: (1) As shown in Figure 10, there is a strong positive correlation between the reciprocal of the curvature of the synchrotron bump at the peak and the intrinsic synchrotron peak frequency. We obtain an empirical formula between them through linear regression analysis. This is consistent with the result of Tramacere et al. (2011). (2) In the observer's coordinate system, the relation between the synchrotron peak frequency and the reciprocal of the curvature of the synchrotron bump is obtained as shown in the following empirical formula:

$$\frac{1}{\beta_{\text{syn}}} = (2.31 \pm 0.14) \log \nu_{\text{peak}}^{\text{syn}} + (-23.65 \pm 2.27) \quad (21)$$

where the Spearman test yields a correlation coefficient  $\rho = 0.88$  and the chance probability is  $P < 10^{-4}$ . Comparing this with the result of Chen (2014), it can be seen that the slope value of Equation (21) there corresponds to three different values,  $5/2$ ,  $10/3$ , and  $2$ , which relate, respectively, to three different mechanisms, i.e., the energy-dependent acceleration probability mechanism, the fluctuation of fractional acceleration gain mechanism, and the stochastic acceleration mechanism (Massaro et al. 2004a; Chen 2014). The particle acceleration mechanism of our sample is closer to the energy-dependent acceleration probability and to the stochastic acceleration mechanism. This shows that there is obvious energy gain diffusion in random acceleration, which leads to momentum diffusion. (3) Unlike the former, the reciprocal of the curvature of the ICs bump at the peak and the intrinsic ICs peak frequency have a weak negative correlation, as shown in Figure 11, and the empirical formula between them is obtained through linear regression analysis, as shown in Table 4. This indicates that the variation of ICs curvature is more complex, which is consistent with our results when the ICs process is in the strong KN scattering region. However, when the ICs process is in the Thomson scattering region,  $\beta_{\text{ic,Th}} \approx 0.5\beta_{\text{syn}}$  (Paggi et al. 2011, 2009; Tramacere et al. 2011). In the KN scattering region,  $1/\beta_{\text{ic}}$  and  $\log \nu_{\text{peak}}^{\text{ic}}$  have a large dispersion, i.e., a weak correlation, due to the KN suppression. We believe that FSRQs and LBLs are more likely to radiate in the Thomson scattering region, while HBLs radiate in the KN scattering region. Moreover, the seed photon sources of FSRQs and most LBLs are complex, and the contribution of the external Compton (EC) process will make the results more complicated.

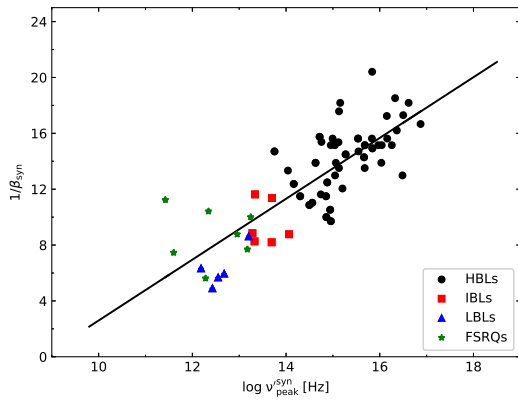


**Figure 10.** The relation between the reciprocal of the curvature of the synchrotron bump at the peak and the intrinsic synchrotron peak frequency.

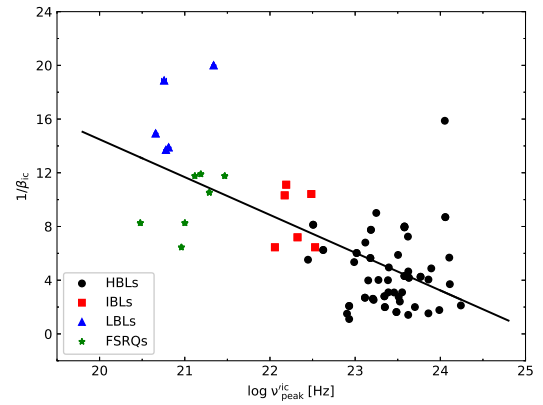


**Figure 11.** The relation between the reciprocal of the curvature of the ICs bump at the peak and the intrinsic ICs peak frequency.

#### 4.5. Intrinsic ICs Peak Frequency versus Peak Lorentz Factor

Figure 12 shows the relation between the peak frequency of the intrinsic ICs spectrum ( $\log \nu_{\text{peak}}^{\text{ic}}$ ) and the peak Lorentz factor ( $\log \gamma_p$ ) of the nonthermal electrons. The Spearman correlation test and linear regression analysis show the following conclusions: (1) There is a strong positive linear correlation between  $\log \nu_{\text{peak}}^{\text{ic}}$  and  $\log \gamma_p$ . According to



Abdo et al. (2010), the Thomson scattering region and the KN scattering region transform in the region  $\gamma=2 \times 10^4$ . It is found that most of the sources in the sample are in the region of  $\gamma > 2 \times 10^4$ , which indicates that the TeV HBLs are in the KN scattering region during the ICs process. In the observer's coordinate system,  $\log \nu_{\text{peak}}^{\text{ic}}$  and  $\log \gamma_p$  have satisfied the following relation:

$$\log \nu_{\text{peak}}^{\text{ic}} = (0.87 \pm 0.02) \log \gamma_p + (20.45 \pm 0.09) \quad (22)$$

where the Spearman test yields a correlation coefficient  $\rho = 0.95$  and the chance probability is  $P < 10^{-4}$ . This result is consistent with the result of Massaro et al. (2006), indicating that when the peak frequency of the ICs spectrum increases with the increase of the peak Lorentz factor, the KN suppression becomes more efficient.

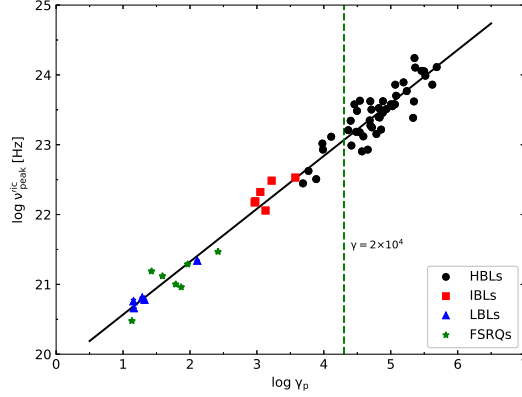


**Figure 12.** The relation between intrinsic ICs peak frequency and peak Lorentz factor.

#### 4.6. Magnetic Field Strength versus Peak Lorentz Factor

As shown in Figure 13, we selected the TeV HBLs in the sample to conduct a correlation test and linear regression analysis between the  $\log B$  and  $\log \gamma_p$  of nonthermal electrons (see Table 4). We can draw the following conclusions: There is a strong linear negative correlation between  $\log B$  and  $\log \gamma_p$ , and the Spearman correlation coefficient is  $-0.79$ . We can obtain the following relation:

$$B = 10^{3.61 \pm 0.81} \gamma_p^{-1.40 \pm 0.81} \quad (23)$$

This shows that the greater the peak Lorentz factor of nonthermal electrons of TeV HBLs, the lower the intensity of the jet magnetic field. According to Equation (A16) and Equation (A17), there is a relation between the jet magnetic field strength ( $B$ ) and the peak Lorentz factor of nonthermal electrons ( $\gamma_p$ ) in the KN scattering region:  $B = K \left( \frac{\nu_{\text{peak}}^{\text{syn}}}{\nu_{\text{peak}}^{\text{ic}}} \right) \gamma_p^{-1}$  where  $K = 14.09 \times 10^{-3/2r}$  ( $r \approx 0.36$  is constant). Compared with Equation (23), the relative error of the exponential part of  $\gamma_p$  is 4%. This suggests that the value of  $\nu_{\text{peak}}^{\text{syn}}/\nu_{\text{peak}}^{\text{ic}}$  will somehow affect the relation between  $B$  and  $\gamma_p$ .

#### 4.7. Radiative Zone Radius versus Peak Lorentz Factor

As shown in Figure 14, we selected the TeV HBLs in the sample to conduct a correlation test and linear regression analysis between the radiating region radius ( $\log R$ ) and the peak Lorentz factor ( $\log \gamma_p$ ) of nonthermal electrons (see Table 4). The following conclusions were drawn: (1) There is no correlation between  $\log R$  and  $\log \gamma_p$ , the Spearman correlation coefficient is 0.03, and the chance probability  $P > 0.05$ . (2) According to Equation (A16) and Equation (A17), there exists the following relation between the radius of the radiation region ( $R$ ) and the peak Lorentz factor ( $\gamma_p$ ) of the nonthermal electrons:

$$\begin{cases} R = K_1 \left( \frac{L_{\text{peak}}^{\text{ic}}}{L_{\text{peak}}^{\text{syn}}} \right) \cdot n^{-1} \cdot \gamma_p^{-2} & \text{(Thomson regime)} \\ R = K_2 \left( \frac{L_{\text{peak}}^{\text{ic}}}{L_{\text{peak}}^{\text{syn}}} \right) \cdot n^{-1} \cdot \gamma_p^2 \cdot B & \text{(KN regime)} \end{cases} \quad (24)$$

where  $K_1 = 9.10 \times 10^{24}$ , and  $K_2 = 5.98 \times 10^{10}$ . In the Thomson scattering region, there is a linear relation between  $\log R$  and  $\log \gamma_p$ . However, in the KN scattering region,  $R$  is not only related to  $\gamma_p$ , but also related to the magnetic

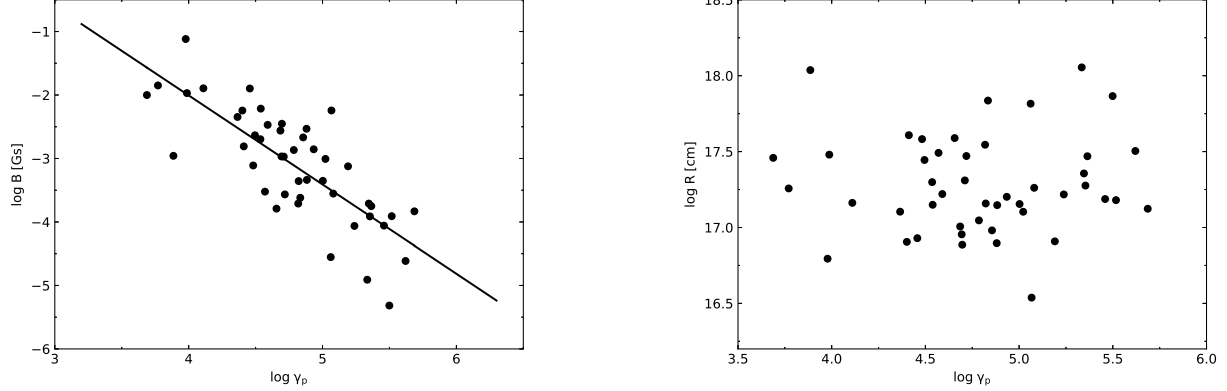


**Figure 13.** The relation between magnetic field strength and peak Lorentz factor for TeV HBLs. **Figure 14.** The relation between radiative zone radius and peak Lorentz factor for TeV HBLs. field strength  $B$ ; therefore  $R$  and  $B$  have an intrinsic degeneracy, and it is impossible to estimate the change of  $\log \gamma_p$  according only to  $\log R$ .

## 5. CONCLUSIONS

In this paper, the average-state multiwavelength energy spectrum data of 65 Fermi TeV blazars were collected and the SED was fitted with a log-parabolic model to obtain the relevant physical parameters. We used the log-parabolic model to adjust the parameters repeatedly so that the reduced chi-square values  $\chi_{\text{syn}}^2$  and  $\chi_{\text{ic}}^2$  were minimized in the coordinate space of  $\log \nu - \log \nu f_\nu$ , and we obtained the average reduced chi-square values of  $\langle \chi_{\text{syn}}^2 \rangle = 0.09$  and  $\langle \chi_{\text{ic}}^2 \rangle = 0.40$ . In order to further study the intrinsic parametric characteristics and to estimate the physical parameters of the jet radiation zone, we selected a samples of 64 classified TeV blazars with redshift. Near the SED peak frequency, the synchrotron region and the ICs region show a log-parabolic shape, and we can calculate the parameters at the peak frequency. We have a total of 17 parameters, including 12 model fitting parameters and 5 indirect calculation parameters, which are listed in Table 1 and 2. We calculated the errors for each model fitting parameter, and the fitting errors were all within the range of  $1\sigma$ . We conducted statistical analysis of these parameters and arrived at the following conclusions:

(1) TeV HBLs can better meet the conditions of the KN scattering region and their parameters can be reasonably estimated by Equation (17), as follows: the Doppler factor,  $5.6 \leq D \leq 31.6$ ; the magnetic field strength,  $6.3 \times 10^{-5} \text{ G} \leq B \leq 1.1 \times 10^{-2} \text{ G}$ ; the radius of the radiative zone,  $7.5 \times 10^{16} \text{ cm} \leq R \leq 4.2 \times 10^{17} \text{ cm}$ ; and the peak Lorentz factor,  $2.5 \times 10^4 \leq \gamma_p \leq 4.0 \times 10^5$ .

(2) The radiation of TeV HBLs satisfies the SSC model well and there is a strong linear positive correlation between the intrinsic synchrotron peak frequency and intrinsic ICs peak frequency. According to the definition of the Compton dominance parameter  $A_C = L_{\text{peak}}^{\text{IC}}/L_{\text{peak}}^{\text{syn}}$  by Finke (2013), we can estimate the mean value of  $A_C$  of different types of sources in the sample as  $\langle A_C \rangle_{\text{HBLs}} = 0.94$ ,  $\langle A_C \rangle_{\text{IBLs}} = 1.30$ ,  $\langle A_C \rangle_{\text{LBLs}} = 1.19$ , and  $\langle A_C \rangle_{\text{FSRQs}} = 9.41$ . According to Ghisellini et al. (2010),  $A_C = L_{\text{peak}}^{\text{IC}}/L_{\text{peak}}^{\text{syn}} = U_{\text{rad}}/U_B$ , where  $U_B$  and  $U_{\text{rad}}$  are the energy density of the magnetic field and the radiation field, respectively. Since  $\langle A_C \rangle_{\text{HBLs}}$  is very small and  $\langle A_C \rangle_{\text{FSRQs}} \approx 10$ , the radiation energy of HBLs is in good agreement with the SSC model, while that of FSRQs is in good agreement with the EC radiation model. When the peak frequency of the ICs spectrum increases with the increase of the peak Lorentz factor, the suppression of the KN effect becomes more efficient.

(3) There is a strong linear positive correlation between the intrinsic ICs peak luminosity and intrinsic  $\gamma$ -ray luminosity and between the intrinsic ICs peak frequency and peak Lorentz factor. We can estimate the parameter values of  $\log L_{\text{peak}}^{\text{ic}}$  and  $\log \nu_{\text{peak}}^{\text{ic}}$  in terms of  $\log L_\gamma$  and  $\log \gamma_p$  by using Equation (20) and (22).

(4) If radio bands are excluded, the negative correlation between the intrinsic peak frequency and the spectral index of each band indicates that the radiation in the radio band is optically thick, while the radiation in the infrared, optical, ultraviolet, and X-ray bands is optically thin. This indicates that the radiating region radius of the radio band is different from that of the other bands. There is radiation loss in each band, but the loss mechanism in the synchrotron region is obviously different from that in the ICs region. The spectra of the source become hard when the

intrinsic synchrotron peak frequencies increase in the synchrotron region. The  $\gamma$ -ray spectrum index shows an inverse L-shaped decrease with the peak frequency in the ICs region.

(5) There is a strong positive correlation between the reciprocal of the curvature of the synchrotron bump at the peak ( $1/\beta_{\text{syn}}$ ) and the peak frequency of intrinsic synchrotron radiation ( $\log \nu_{\text{peak}}^{\text{syn}}$ ). According to Equation (21), we can use the energy-dependent acceleration probability and stochastic acceleration mechanism to explain this correlation, i.e., there is obvious energy gain diffusion in stochastic acceleration, which leads to momentum diffusion. There is a weak negative correlation between the reciprocal of the curvature of the ICs bump at the peak ( $1/\beta_{\text{ic}}$ ) at the peak and the ICs peak frequency ( $\log \nu_{\text{peak}}^{\text{ic}}$ ). We consider that ICs of FSRQs and LBLs is more likely to occur in the Thomson scattering region, while that of HBLs is more likely to occur in the KN scattering region. At the same time, the contribution of EC scattering may influence the results to some extent. In addition, if the combination of acceleration and cooling effect is considered, the interpretation of ICs curvature will be more complicated.

(6) The larger the peak Lorentz factor of nonthermal electrons in TeV HBLs, the lower the intensity of the jet magnetic field. The value of  $\nu_{\text{peak}}^{\text{syn}}/\nu_{\text{peak}}^{\text{ic}}$  has some effect on the relationship between the two parameters.

(7) In the KN scattering region, R is not only related to  $\gamma_{\text{p}}$ , but also related to the magnetic field strength B; therefore R and B have an intrinsic degeneracy, and it is impossible to estimate the change of  $\log \gamma_{\text{p}}$  according only to  $\log R$ .

Due to the limited number of Fermi TeV blazars, and to the fact that the energy spectrum data are long-interval average SEDs and most of them are from HBLs, our analysis conclusions may be more suitable to objects of the HBL type. Therefore, the influence of EC scattering has not been fully considered. According to the formulas in Chen (2018) and Chen & Bai (2011), we can get the peak frequency and peak luminosity of the EC process as follows:  $\nu_{\text{peak}}^{\text{ec}} \approx (4/3)\nu_{\text{ext}}\gamma_{\text{p,Th}}^2\Gamma$  and  $L_{\text{peak,Th}}^{\text{ec}} \approx (17e^2/(6\pi m_e^2 c^2))(u_{\text{ext}}/\nu_{\text{ext}}^2)(\nu_{\text{peak,Th}}^{\text{ec}}/\nu_{\text{peak}}^{\text{syn}})^2 L_{\text{peak}}^{\text{syn}}$ , where  $\Gamma$  is the bulk Lorentz factor, we take  $\Gamma \approx D_{\text{Th}}$ , and  $\gamma_{\text{p,Th}}$  is the peak Lorentz factor in the Thomson scattering regime. We substitute in Equation (13) and Equation (16) to derive the following formula:

$$B = 212.62 \left( \frac{\nu_{\text{peak}}^{\text{ec}}}{10^{22} \text{Hz}} \right)^{-\frac{1+2\xi}{2(1+\xi)}} \left( \frac{10^{15} \text{Hz}}{\nu_{\text{peak}}^{\text{syn}}} \right)^{-\frac{1+2\xi}{2(1+\xi)}} \left( \frac{L_{\text{peak}}^{\text{syn}}}{10^{45} \text{erg s}^{-1}} \right)^{\frac{1}{2(1+\xi)}} \left( \frac{10^{45} \text{erg s}^{-1}}{L_{\text{peak}}^{\text{ssc}}} \right)^{\frac{1}{4(1+\xi)}} \left( \frac{\Delta t}{1 \text{day}} \right)^{-\frac{1}{2(1+\xi)}} \left( \frac{\nu_{\text{ext}}}{2 \times 10^{15} \text{Hz}} \right)^{\frac{1+2\xi}{2(1+\xi)}} 10^{\frac{1-2\xi}{10\beta_{\text{syn}}(1+\xi)}} \beta_{\text{syn}}^{-\frac{1}{8(1+\xi)}} (1+z)^{\frac{\xi-1}{\xi+1}} \text{Gs} \quad (25)$$

where  $\nu_{\text{ext}}$  is the modified dominant frequency of external radiation in the jet. If we consider that the broad-line region (BLR) provides the external photon field, we can take  $\nu_{\text{ext-BLR}} \approx 2 \times 10^{15} \text{Hz}$ . The high-energy observation data points of average-state multiwavelength SED collected in our sample are few, so the position of the EC peak frequency  $\nu_{\text{peak}}^{\text{ec}}$  cannot be given. According to Equation (25), we estimate the physical parameters of LBLs and FSRQs in the case of EC scattering, as shown in Table 5.

**Table 5.** Physical parameters of LBLs and FSRQs in EC case

TeV Source Name (1)	Class (2)	$\log \nu_{\text{peak}}^{\text{ec}}$ (3)	$\log B$ (4)	$\log \gamma_{\text{p}}$ (5)
OJ 287	LBLs	23.02	0.30	3.13
S4 0954 + 65	LBLs	23.19	-0.03	3.21
AP Lib	LBLs	21.61	0.92	2.77
OT 081	LBLs	22.61	0.16	3.06
BL Lacertae	LBLs	23.35	-0.21	3.35
S3 0218 + 35	FSRQs	22.39	1.49	2.42
PKS 0736 + 017	FSRQs	20.70	1.41	2.43
TON 0599	FSRQs	23.74	-0.25	3.41
4C + 21.35	FSRQs	22.02	1.07	2.88
3C 279	FSRQs	23.20	-0.20	3.01
PKS 1441 + 25	FSRQs	22.27	0.07	2.94
PKS 1510 - 089	FSRQs	21.58	0.67	2.72

Note. Column (1) gives the TeV source name. Column (2) gives the class designation for the source. Column (3)-(5) give the peak frequency of EC scattering obtained from the Thomson scattering region  $\log \nu_{\text{peak}}^{\text{ec}}$  (Hz), the magnetic field strength  $\log B$  (G), and the peak Lorentz factor  $\log \gamma_{\text{p}}$ .

According to the calculation results, for LBLs and FSRQs, if the EC effect is taken into account, the average magnetic

field strength of LBLs and FSRQs is  $\langle \log B \rangle_{\text{LBLs}} = 0.23\text{G}$  and  $\langle \log B \rangle_{\text{FSRQs}} = 0.61\text{G}$ ; the average values of the peak Lorentz factors are  $\langle \log \gamma_p \rangle_{\text{LBLs}} = 3.10$  and  $\langle \log \gamma_p \rangle_{\text{FSRQs}} = 2.83$ . Compared with the results in [Chen \(2018\)](#), in the Thomson case, when the influence of the EC process on LBLs and FSRQs is considered, the values of the magnetic field strength and peak Lorentz factor can reach the reasonable parameter range of  $0 \leq \log B \leq 1$  and  $2 \leq \log \gamma_p \leq 3$  ([Ghisellini & Tavecchio 2015](#)). In addition, the log-parabola model does not consider the combination of acceleration and cooling effects on the curvature of the ICs energy spectrum, and we leave this issue for future work.

### ACKNOWLEDGEMENTS

We thank the anonymous referee for valuable comments and suggestions. This work was partially supported by the National Natural Science Foundation of China (grant Nos.11763005 and 11873043), and the Science and Technology Foundation of Guizhou Province (QKHJC[2019]1290). This work is also supported by the Graduate Research Foundation of Yunnan Normal University. The authors would like to express their gratitude to EditSprings (<https://www.editsprings.com/>) for the expert linguistic services provided.

### APPENDIX

#### A. DERIVATION OF JET RADIATION ZONE PARAMETERS

In order to further study the physical properties of the jet radiation zone, four parameters are introduced in Section 2.2, which are as follows: the Doppler factor  $D$ ; the peak Lorentz factor  $\gamma_p$  of nonthermal electrons; the radiation zone radius  $R$ ; and the magnetic field of the jet  $B$ .

In the case of stochastic acceleration, and monoenergetic and instantaneous injection, the EED in the jet can be written as ([Kardashev 1962](#); [Massaro et al. 2006](#); [Paggi et al. 2009, 2011](#); [Zheng et al. 2018](#))

$$N(\gamma) = N_0 \left( \frac{\gamma}{\gamma_0} \right)^{-s-r \log\left(\frac{\gamma}{\gamma_0}\right)} \quad (\text{A1})$$

where  $\gamma_0$  is the initial electron Lorentz factor,  $s$  is the electron spectrum index,  $r$  is the electron spectrum curvature,  $N_0 = \frac{n}{\gamma_0} 10^{-\frac{(s-1)^2}{4r}} \sqrt{\frac{2}{\pi}} \frac{1}{\sqrt{\ln 10}}$  is the normalization constant in units of  $\text{cm}^{-3}$ ,  $n = \int N(\gamma) d\gamma$  is the particle number density, and  $\gamma$  is the electronic Lorentz factor.

The traditional single-zone uniform SSC model assumes that there is a homogeneous spherical radiation zone (or blob) with radius  $R$  moving along the jet orientation at a relativistic velocity  $v = \beta'c$  ( $c$  is the speed of light, and  $\Gamma = 1/\sqrt{1-\beta'^2}$  is the bulk Lorentz factor), surrounded by a magnetic field  $B$  ([Kang 2017](#); [Ghisellini et al. 2010](#); [Arsioli & Chang 2018](#)). The Doppler factor is denoted by

$$D = \frac{1}{\Gamma(1 - \beta' \cos \theta)} \quad (\text{A2})$$

We assume that when the relativistic jet has a small viewing angle of  $\theta \leq 1/\Gamma$ , the above equation is written as  $D \approx \Gamma$ .

In the co-moving coordinate system, the luminosity can be expressed as ([Paggi et al. 2011](#); [Chen 2018](#))

$$L'(\nu') = \frac{4}{3} \pi R^3 \frac{\nu' j_{\nu'}}{\tau_{\nu'}} \left[ 1 - \frac{1 - e^{-2\tau_{\nu'}}(1 + 2\tau_{\nu'})}{2\tau_{\nu'}^2} \right] \quad (\text{A3})$$

where  $j_{\nu'}$  is the emission coefficient,  $\tau_{\nu'} = k_{\nu'} R$  is the optical depth of the source, and  $k_{\nu'}$  is the absorption coefficient. For optically thin sources ( $\tau_{\nu'} \ll 1$ ), the above equation can be written as  $L'(\nu') = \frac{4}{3} \pi R^3 \cdot 4\pi \nu' j(\nu')$ .

The radiation is usually optically thin at the peak frequency ([Chen 2018](#)). According to  $L'(\nu') = 4\pi d_L^2 \nu f'(\nu')$ , we can get the following formula:

$$f'(\nu') = \frac{1}{3} \frac{4\pi R^3}{d_L^2} j(\nu') \quad (\text{A4})$$

For the emission coefficient of synchrotron radiation, we have

$$j_{\text{syn}}(\nu') = \frac{1}{4\pi} \int N(\gamma) \frac{dP_{\text{syn}}}{d\nu'} d\gamma \quad (\text{A5})$$

where  $P_{\text{syn}} = \frac{4}{3}\sigma_{\text{T}}c\beta^2\gamma^2u_{\text{B}}$  is the emitted power by the synchrotron radiation of a single electron,  $u_{\text{B}} = \frac{B^2}{8\pi}$  is the energy density of the magnetic field, and  $\sigma_{\text{T}} = \frac{8\pi e^4}{3m^2c^4}$  is the Thomson cross section. For relativistic electrons, we take  $\beta \approx 1$  (Rybicki & Lightman 1979).

In Equation (A5), we introduce a delta approximated by

$$\frac{dP_{\text{syn}}}{d\nu'} = P_{\text{syn}}\delta(\nu' - \gamma^2\nu_c) \quad (\text{A6})$$

where  $\nu_c = 0.29(3/2)\nu_{\text{L}}\sin\theta$  is the characteristic frequency;  $\nu_{\text{L}} = \frac{eB}{2\pi m_e c}$  is the Larmor frequency of relativistic electrons, and  $\theta$  is the angle between  $\vec{v}$  and  $\vec{B}$  (Rybicki & Lightman 1979; Paggi et al. 2011).

Substitute Equation (A1), Equation (A6), and Equation(A5) into Equation (A4), and we get the synchrotron radiation flux:

$$f'_{\text{syn}}(\nu') = G_1 \cdot B \frac{R^3}{d_L^2} \sqrt{\frac{\nu'}{\nu_c}} N \left( \sqrt{\frac{\nu'}{\nu_c}} \right) \quad (\text{A7})$$

where  $G_1 \approx 0.156 \frac{\sigma_{\text{T}} m c^2}{e}$  is a constant.

According to Equation (A4), the synchrotron luminosity is calculated as

$$L'_{\text{syn}}(\nu') = G_2 \cdot n \sqrt{r} 10^{-\frac{(s-1)^2}{4r}} \gamma_0^2 R^3 B^2 \left( \frac{\nu'}{\nu'_0} \right)^{-\frac{(s-3)}{2} - \frac{r}{4} \log\left(\frac{\nu'}{\nu'_0}\right)} \quad (\text{A8})$$

where  $G_2 \approx 0.051\sigma_{\text{T}}c$  is a constant and  $\nu'_0 = \gamma_0^2\nu_c$ .

For ICs, we consider that the ambient soft photons originate from synchrotron in the jet and have the same electron number distribution as those in SSC radiation. The SSC emission coefficient can be expressed as

$$j_{\text{ic}}(\nu') = \frac{1}{4\pi} \int N(\gamma) \frac{dP_{\text{ic}}}{d\nu'} d\gamma \quad (\text{A9})$$

where  $P_{\text{ic}} = \frac{4}{3}c\sigma_{\text{T}}\gamma^2\beta^2u_{\text{ph}}$  is the ICs emitted power by an electron,  $u_{\text{ph}} = m_e c^2 \int \varepsilon_{\text{syn}} n(\varepsilon_{\text{syn}}) d\varepsilon_{\text{syn}}$  is the photon energy density,  $\varepsilon_{\text{syn}} = \frac{h\nu_{\text{syn}}}{m_e c^2}$  is the synchrotron photon energy, and  $n(\varepsilon_{\text{syn}})$  is the seed photon number density. In the Equation (A9), we introduce a delta approximated by

$$\frac{dP_{\text{ic}}}{d\nu'} = P_{\text{ic}}\delta\left(\nu' - \frac{4}{3}\gamma^2\nu'^{\text{syn}}_{\text{peak}}\right) \quad (\text{A10})$$

where  $\nu'^{\text{syn}}_{\text{peak}} = \nu_c \gamma_0^2 10^{\frac{3-s}{r}}$  is the synchrotron radiation peak frequency.

Based on the scattered photon energy, ICs is divided into the Thomson scattering region ( $E_{\text{ph}} \ll m_e c^2$ ) and the KN scattering region ( $E_{\text{ph}} \gg m_e c^2$ ).

For the optically thin case, we substitute Equation (A1), Equation (A10), and Equation (A9) into Equation (A4), and we get the SSC radiation flux in the Thomson scattering region as

$$f'_{\text{ic,Th}}(\nu') = \sigma_{\text{T}}c \cdot B \frac{R^3}{d_L^2} \frac{u_{\text{ph}}}{\nu'^{\text{syn}}_{\text{peak}}} \sqrt{\frac{3\nu'}{4\nu_c}} N \left( \sqrt{\frac{3\nu'}{4\nu_c}} \right) \quad (\text{A11})$$

where  $u_{\text{ph}}^{\text{Th}}(\nu'_0) = h \int \nu' \bar{N}_{\text{syn}}(\nu'_0) \Omega(\nu', \nu'_0, \gamma) d\nu'_0$  is the synchrotron photon energy density,  $\Omega(\nu', \nu'_0, \gamma)$  is the Compton kernel function given by Zheng et al. (2019), and  $\bar{N}_{\text{syn}}(\nu'_0) = \frac{3}{4} \frac{R}{c} \frac{j_{\text{syn}}(\nu'_0)}{h\nu'_0}$  is the average synchrotron photon density (Rybicki & Lightman 1979; Paggi et al. 2011). In the Thomson scattering region, the SSC radiation luminosity can be expressed as

$$L'_{\text{ic,Th}}(\nu') = G_3 \cdot n^2 \sqrt{r} 10^{-\frac{(s-1)^2}{4r}} 10^{\frac{2-s}{r}} \gamma_0^4 R^4 B^2 \left( \frac{\nu'}{\hat{\nu}'_0} \right)^{-\frac{(s-3)}{2} - \frac{r}{4} \log\left(\frac{\nu'}{\hat{\nu}'_0}\right)} \quad (\text{A12})$$

where  $G_3 = 0.479 \frac{e^4 r_0^2}{m^2 c^3}$  is a constant and  $\hat{\nu}'_0 = \frac{4}{3} \nu_c \gamma_0^4 10^{\frac{3-s}{r}}$ .

For extreme KN scattering, we rewrite Equation (A9) as

$$j_{\text{ic,KN}}(\nu') = h \int d\gamma N(\gamma) \int \nu' \bar{N}_{\text{syn}}(\nu'_0) \Omega(\nu', \nu'_0, \gamma) d\nu'_0 \quad (\text{A13})$$

where we introduce a delta approximated by  $\Omega(\nu', \nu'_0, \gamma) = \frac{2\pi r_0^2 c \nu'}{\gamma^2} \delta\left(\gamma - \frac{h\nu'}{mc^2}\right)$ ,  $\bar{N}_{\text{syn}}(\nu'_0) = \frac{3}{4} \frac{R}{c} \frac{j_{\text{syn}}(\nu'_0)}{h\nu'_0}$  is the average synchrotron photon density, and  $r_0 = \frac{e^2}{m_e c^2}$  is the classical radius of the electron (Rybicki & Lightman 1979; Paggi et al. 2011).

In the KN scattering region, the SSC radiation luminosity can be expressed as

$$L'_{\text{ic,KN}}(\nu') = G_4 \cdot n^2 \sqrt{r} 10^{-\frac{(s-1)^2}{4r}} R^4 B \left(\frac{\nu'}{\hat{\nu}'_a}\right)^{-(s-1)-r \log\left(\frac{\nu'}{\hat{\nu}'_a}\right)} \quad (\text{A14})$$

where  $G_4 = 130.428 \frac{e^3}{h} r_0^2$  is a constant and  $\hat{\nu}'_a = \frac{\gamma_0 m c^2}{h}$  (Chen 2018).

From the equation

$$\log\left(\frac{N(\gamma)}{N_0}\right) = -r \log^2\left(\frac{\gamma}{\gamma_0}\right) - s \log\left(\frac{\gamma}{\gamma_0}\right) \quad (\text{A15})$$

where setting  $\gamma_0 = \gamma_p$ , we can get  $\gamma_p = \gamma_0 10^{-\frac{s}{2r}}$  and  $N_p = N_0 10^{\frac{s^2}{4r}}$ .

We find that Equation (A8), Equation (A12) and Equation (A14) all have the form of Equation (A1). According to the result of Equation (A15), we can get  $\nu_{\text{peak}}^{\text{syn}}$ ,  $\nu_{\text{peak}}^{\text{ic}}$ ,  $L_{\text{peak}}^{\text{syn}}$ ,  $L_{\text{peak,Th}}^{\text{ic}}$  and  $L_{\text{peak,KN}}^{\text{ic}}$ .

In the Thomson scattering region, we get

$$\begin{cases} \nu_{\text{peak}}^{\text{syn}} = c_1 \cdot B \gamma_p^2 10^{\frac{1}{r}} \\ L_{\text{peak}}^{\text{syn}} = c_2 \cdot n \sqrt{r} \gamma_p^2 R^3 B^2 \\ \nu_{\text{peak,Th}}^{\text{ic}} = c_3 \cdot B \gamma_p^4 10^{\frac{2}{r}} \\ L_{\text{peak,Th}}^{\text{ic}} = c_4 \cdot n^2 \sqrt{r} \gamma_p^4 R^4 B^2 \end{cases} \quad (\text{A16})$$

where  $c_1 = 9.942 \times 10^5$ ,  $c_2 = 8.239 \times 10^{-16}$ ,  $c_3 = 1.326 \times 10^6$ , and  $c_4 = 9.056 \times 10^{-41}$  are constant.

In the KN scattering region, we get

$$\begin{cases} \nu_{\text{peak}}^{\text{syn}} = c_1 \cdot B \gamma_p^2 10^{\frac{1}{r}} \\ L_{\text{peak}}^{\text{syn}} = c_2 \cdot n \sqrt{r} \gamma_p^2 R^3 B^2 \\ \nu_{\text{peak,KN}}^{\text{ic}} = c_5 \cdot \gamma_p 10^{-\frac{1}{2r}} \\ L_{\text{peak,KN}}^{\text{ic}} = c_6 \cdot n^2 \sqrt{r} R^4 B \end{cases} \quad (\text{A17})$$

where  $c_5 = 1.236 \times 10^{20}$ , and  $c_6 = 1.378 \times 10^{-26}$  are constant.

According to the research of Massaro et al. (2004b, 2008b,a), the relation between the electron spectrum curvature ( $r$ ) and the curvature of the synchrotron bump ( $\beta_{\text{syn}}$ ) is  $r \approx 5\beta_{\text{syn}}$ . Thus, if we solve Equation (A16), in the Thomson scattering region, we can get

$$\gamma_p = 8660.3 \left( \frac{\nu_{\text{peak,Th}}^{\text{ic}}}{10^{23} \text{Hz}} \cdot \frac{10^{15} \text{Hz}}{\nu_{\text{peak}}^{\text{syn}}} \right)^{\frac{1}{2}} 10^{-\frac{1}{10\beta_{\text{syn}}}} \quad (\text{A18})$$

$$B = 13.4109 \left( \frac{\nu_{\text{peak}}^{\text{syn}}}{10^{15} \text{Hz}} \right)^2 \left( \frac{10^{23} \text{Hz}}{\nu_{\text{peak,Th}}^{\text{ic}}} \right) \quad (\text{A19})$$

$$R = 2.7235 \times 10^{16} \left( \frac{\nu_{\text{peak,Th}}^{\text{ic}}}{10^{23} \text{Hz}} \right) \left( \frac{10^{15} \text{Hz}}{\nu_{\text{peak}}^{\text{syn}}} \right)^2 \left( \frac{L_{\text{peak}}^{\text{syn}}}{10^{45} \text{erg s}^{-1}} \right) \left( \frac{10^{45} \text{erg s}^{-1}}{L_{\text{peak,Th}}^{\text{ic}}} \right)^{\frac{1}{2}} \quad (\text{A20})$$

By substituting Equation (13), Equation (15) and Equation (A20) into  $R = c\Delta t \frac{D_{\text{var}}}{(1+z)}$  (e.g., Rybicki & Lightman (1979)), we obtain

$$D_{\text{Th}} = (247.2179)^{\frac{1}{4\xi}} (1+z)^{\frac{1-\xi}{\xi}} \left( \frac{10^{45} \text{erg s}^{-1}}{L_{\text{peak,Th}}^{\text{ic}}} \right)^{\frac{1}{4\xi}} \left( \frac{L_{\text{peak}}^{\text{syn}}}{10^{45} \text{erg s}^{-1}} \right)^{\frac{1}{2\xi}} \left( \frac{\nu_{\text{peak,Th}}^{\text{ic}}}{10^{23} \text{Hz}} \right)^{\frac{1}{2\xi}} \left( \frac{10^{15} \text{Hz}}{\nu_{\text{peak}}^{\text{syn}}} \right)^{\frac{1}{\xi}} \left( \frac{1 \text{ day}}{\Delta t} \right)^{\frac{1}{2\xi}} (\beta_{\text{syn}})^{\frac{1}{8\xi}} \quad (\text{A21})$$

where  $\xi = 1 + \frac{2\alpha_{\nu_{\text{peak}}^{\text{syn}}} - \alpha_{\nu_{\text{peak}}^{\text{ic}}}}{4}$ , and  $\Delta t$  is the minimum timescale of variation.

Then, if we solve Equation (A17), in the KN scattering region we can get

$$\gamma_p = 809.332 \left( \frac{\nu_{\text{peak,KN}}^{\text{ic}}}{10^{23} \text{Hz}} \right) 10^{\frac{1}{10\beta_{\text{syn}}}} \quad (\text{A22})$$

$$B = 1.5356 \times 10^3 \left( \frac{\nu_{\text{peak}}^{\text{syn}}}{10^{15} \text{Hz}} \right) \left( \frac{10^{23} \text{Hz}}{\nu_{\text{peak,KN}}^{\text{ic}}} \right)^2 10^{-\frac{2}{5\beta_{\text{syn}}}} \quad (\text{A23})$$

$$R = 7.6456 \times 10^{13} (\beta_{\text{syn}})^{-\frac{1}{4}} 10^{\frac{2}{5\beta_{\text{syn}}}} \left( \frac{\nu_{\text{peak,KN}}^{\text{ic}}}{10^{23} \text{Hz}} \right) \left( \frac{10^{15} \text{Hz}}{\nu_{\text{peak}}^{\text{syn}}} \right)^{\frac{3}{2}} \left( \frac{L_{\text{peak}}^{\text{syn}}}{10^{45} \text{erg s}^{-1}} \right) \left( \frac{10^{45} \text{erg s}^{-1}}{L_{\text{peak,KN}}^{\text{ic}}} \right)^{\frac{1}{2}} \quad (\text{A24})$$

By substituting Equation (13), Equation (15) and Equation (A24) into  $R = c\Delta t \frac{D_{\text{var}}}{(1+z)}$  (e.g., Rybicki & Lightman (1979)), we obtain

$$D_{\text{KN}} = (0.0295)^{\frac{1}{\zeta}} \left( (1+z)^{\frac{\zeta-2}{\zeta}} \right) \left( \frac{L_{\text{peak}}^{\text{syn}}}{10^{45} \text{erg s}^{-1}} \right)^{\frac{1}{\zeta}} \left( \frac{10^{45} \text{erg s}^{-1}}{L_{\text{peak,KN}}^{\text{ic}}} \right)^{\frac{1}{2\zeta}} \left( \frac{10^{15} \text{Hz}}{\nu_{\text{peak}}^{\text{syn}}} \right)^{\frac{3}{2\zeta}} \left( \frac{\nu_{\text{peak,KN}}^{\text{ic}}}{10^{23} \text{Hz}} \right)^{\frac{1}{\zeta}} \left( \frac{1 \text{day}}{\Delta t} \right)^{\frac{1}{\zeta}} 10^{\frac{2}{5\beta_{\text{syn}}\zeta}} (\beta_{\text{syn}})^{-\frac{1}{4\zeta}} \quad (\text{A25})$$

where  $\zeta = \frac{5+2\alpha_{\nu_{\text{peak}}^{\text{syn}}} - \alpha_{\nu_{\text{peak}}^{\text{ic}}}}{2}$ , and  $\Delta t$  is the minimum timescale.

## REFERENCES

- Abdo, A. A., Ackermann, M., Agudo, I., et al. 2010, ApJ, 716, 30, doi: [10.1088/0004-637X/716/1/30](https://doi.org/10.1088/0004-637X/716/1/30)
- Abdollahi, S., Acero, F., Ackermann, M., et al. 2020, ApJS, 247, 33, doi: [10.3847/1538-4365/ab6bcb](https://doi.org/10.3847/1538-4365/ab6bcb)
- Abramowski, A., Aharonian, F., Ait Benkhali, F., et al. 2015, ApJ, 802, 65, doi: [10.1088/0004-637X/802/1/65](https://doi.org/10.1088/0004-637X/802/1/65)
- Ackermann, M., Ajello, M., Allafort, A., et al. 2012, Science, 338, 1190, doi: [10.1126/science.1227160](https://doi.org/10.1126/science.1227160)
- Aharonian, F. A., Akhperjanian, A. G., Barrio, J. A., et al. 2001, A&A, 366, 62, doi: [10.1051/0004-6361:20000098](https://doi.org/10.1051/0004-6361:20000098)
- Ajello, M., Angioni, R., Axelsson, M., et al. 2020, ApJ, 892, 105, doi: [10.3847/1538-4357/ab791e](https://doi.org/10.3847/1538-4357/ab791e)
- Aleksić, J., Ansoldi, S., Antonelli, L. A., et al. 2014, A&A, 567, A135, doi: [10.1051/0004-6361/201423364](https://doi.org/10.1051/0004-6361/201423364)
- Arsioli, B., & Chang, Y. L. 2018, A&A, 616, A63, doi: [10.1051/0004-6361/201833005](https://doi.org/10.1051/0004-6361/201833005)
- Baloković, M., Paneque, D., Madejski, G., et al. 2016, ApJ, 819, 156, doi: [10.3847/0004-637X/819/2/156](https://doi.org/10.3847/0004-637X/819/2/156)
- Biteau, J., & Williams, D. A. 2015, ApJ, 812, 60, doi: [10.1088/0004-637X/812/1/60](https://doi.org/10.1088/0004-637X/812/1/60)
- Blażejowski, M., Blaylock, G., Bond, I. H., et al. 2005, ApJ, 630, 130, doi: [10.1086/431925](https://doi.org/10.1086/431925)
- Chen, L. 2014, ApJ, 788, 179, doi: [10.1088/0004-637X/788/2/179](https://doi.org/10.1088/0004-637X/788/2/179)
- . 2018, ApJS, 235, 39, doi: [10.3847/1538-4365/aab8fb](https://doi.org/10.3847/1538-4365/aab8fb)
- Chen, L., & Bai, J. M. 2011, ApJ, 735, 108, doi: [10.1088/0004-637X/735/2/108](https://doi.org/10.1088/0004-637X/735/2/108)
- Cheng, K. S., Zhang, X., & Zhang, L. 2000, ApJ, 537, 80, doi: [10.1086/309003](https://doi.org/10.1086/309003)
- Costamante, L. 2020, MNRAS, 491, 2771, doi: [10.1093/mnras/stz3018](https://doi.org/10.1093/mnras/stz3018)
- Czerny, B., & Elvis, M. 1987, ApJ, 321, 305, doi: [10.1086/165630](https://doi.org/10.1086/165630)
- Fallah Ramazani, V., Lindfors, E., & Nilsson, K. 2017, A&A, 608, A68, doi: [10.1051/0004-6361/201730505](https://doi.org/10.1051/0004-6361/201730505)
- Fan, J., Yang, J. H., Zhang, J.-Y., et al. 2013a, PASJ, 65, 25, doi: [10.1093/pasj/65.2.25](https://doi.org/10.1093/pasj/65.2.25)
- Fan, J.-H., Bastieri, D., Yang, J.-H., et al. 2014, Research in Astronomy and Astrophysics, 14, 1135, doi: [10.1088/1674-4527/14/9/004](https://doi.org/10.1088/1674-4527/14/9/004)
- Fan, J.-H., Huang, Y., He, T.-M., et al. 2009, PASJ, 61, 639, doi: [10.1093/pasj/61.4.639](https://doi.org/10.1093/pasj/61.4.639)
- Fan, J. H., Yang, J. H., Liu, Y., Cai, W., & Lin, C. 2015, International Journal of Modern Physics A, 30, 1545020, doi: [10.1142/S0217751X15450207](https://doi.org/10.1142/S0217751X15450207)
- Fan, J.-H., Yang, J.-H., Liu, Y., & Zhang, J.-Y. 2013b, Research in Astronomy and Astrophysics, 13, 259, doi: [10.1088/1674-4527/13/3/002](https://doi.org/10.1088/1674-4527/13/3/002)
- Fan, J. H., Yang, J. H., Yuan, Y. H., Wang, J., & Gao, Y. 2012, ApJ, 761, 125, doi: [10.1088/0004-637X/761/2/125](https://doi.org/10.1088/0004-637X/761/2/125)
- Fan, J. H., Yang, J. H., Liu, Y., et al. 2016, ApJS, 226, 20, doi: [10.3847/0067-0049/226/2/20](https://doi.org/10.3847/0067-0049/226/2/20)
- Fan, J. H., Yang, J. H., Xiao, H. B., et al. 2017, ApJL, 835, L38, doi: [10.3847/2041-8213/835/2/L38](https://doi.org/10.3847/2041-8213/835/2/L38)

- Feigelson, E. D., & Babu, G. J. 2012, *Modern Statistical Methods for Astronomy*
- Finke, J. D. 2013, *ApJ*, 763, 134, doi: [10.1088/0004-637X/763/2/134](https://doi.org/10.1088/0004-637X/763/2/134)
- Finke, J. D., Razzaque, S., & Dermer, C. D. 2010, *ApJ*, 712, 238, doi: [10.1088/0004-637X/712/1/238](https://doi.org/10.1088/0004-637X/712/1/238)
- Fossati, G., Maraschi, L., Celotti, A., Comastri, A., & Ghisellini, G. 1998, *MNRAS*, 299, 433, doi: [10.1046/j.1365-8711.1998.01828.x](https://doi.org/10.1046/j.1365-8711.1998.01828.x)
- Ghisellini, G., Maraschi, L., Tanzi, E. G., & Treves, A. 1986, *ApJ*, 310, 317, doi: [10.1086/164684](https://doi.org/10.1086/164684)
- Ghisellini, G., Padovani, P., Celotti, A., & Maraschi, L. 1993, *ApJ*, 407, 65, doi: [10.1086/172493](https://doi.org/10.1086/172493)
- Ghisellini, G., & Tavecchio, F. 2015, *MNRAS*, 448, 1060, doi: [10.1093/mnras/stv055](https://doi.org/10.1093/mnras/stv055)
- Ghisellini, G., Tavecchio, F., Foschini, L., et al. 2010, *MNRAS*, 402, 497, doi: [10.1111/j.1365-2966.2009.15898.x](https://doi.org/10.1111/j.1365-2966.2009.15898.x)
- Giommi, P., Padovani, P., Polenta, G., et al. 2012, *MNRAS*, 420, 2899, doi: [10.1111/j.1365-2966.2011.20044.x](https://doi.org/10.1111/j.1365-2966.2011.20044.x)
- H. E. S. S. Collaboration, Abramowski, A., Acero, F., et al. 2010, *A&A*, 520, A83, doi: [10.1051/0004-6361/201014484](https://doi.org/10.1051/0004-6361/201014484)
- HESS Collaboration, Abramowski, A., Acero, F., et al. 2013, *MNRAS*, 434, 1889, doi: [10.1093/mnras/stt1081](https://doi.org/10.1093/mnras/stt1081)
- Hovatta, T., Valtaoja, E., Tornikoski, M., & Lähteenmäki, A. 2009, *A&A*, 494, 527, doi: [10.1051/0004-6361:200811150](https://doi.org/10.1051/0004-6361:200811150)
- Huang, L. H., Jiang, D. R., & Cao, X. 1999, *A&A*, 341, 74, <https://arxiv.org/abs/astro-ph/9809251>
- Ivezić, Ž., Connelly, A. J., Vand erPlas, J. T., & Gray, A. 2014, *Statistics, Data Mining, and Machine Learning in Astronomy*
- Kang, S.-J. 2017, *ApJ*, 837, 38, doi: [10.3847/1538-4357/aa6005](https://doi.org/10.3847/1538-4357/aa6005)
- Kang, S.-J., Chen, L., & Wu, Q. 2014, *ApJS*, 215, 5, doi: [10.1088/0067-0049/215/1/5](https://doi.org/10.1088/0067-0049/215/1/5)
- Kang, S.-J., Wu, Q., Zheng, Y.-G., et al. 2018, *Research in Astronomy and Astrophysics*, 18, 056, doi: [10.1088/1674-4527/18/5/56](https://doi.org/10.1088/1674-4527/18/5/56)
- Kardashev, N. S. 1962, *Soviet Ast.*, 6, 317
- Kembhavi, A. K., & Narlikar, J. V. 1999, *Quasars and active galactic nuclei : an introduction*
- Lähteenmäki, A., & Valtaoja, E. 1999, *ApJ*, 521, 493, doi: [10.1086/307587](https://doi.org/10.1086/307587)
- Lin, C., & Fan, J.-H. 2016, *Research in Astronomy and Astrophysics*, 16, 103, doi: [10.1088/1674-4527/16/7/103](https://doi.org/10.1088/1674-4527/16/7/103)
- . 2018, *Research in Astronomy and Astrophysics*, 18, 120, doi: [10.1088/1674-4527/18/10/120](https://doi.org/10.1088/1674-4527/18/10/120)
- Lin, C., Fan, J.-H., & Xiao, H.-B. 2017, *Research in Astronomy and Astrophysics*, 17, 066, doi: [10.1088/1674-4527/17/7/66](https://doi.org/10.1088/1674-4527/17/7/66)
- Maraschi, L., Ghisellini, G., & Celotti, A. 1992, *ApJL*, 397, L5, doi: [10.1086/186531](https://doi.org/10.1086/186531)
- Massaro, E., Perri, M., Giommi, P., & Nesci, R. 2004a, *A&A*, 413, 489, doi: [10.1051/0004-6361:20031558](https://doi.org/10.1051/0004-6361:20031558)
- Massaro, E., Perri, M., Giommi, P., Nesci, R., & Verrecchia, F. 2004b, *A&A*, 422, 103, doi: [10.1051/0004-6361:20047148](https://doi.org/10.1051/0004-6361:20047148)
- Massaro, E., Tramacere, A., Perri, M., Giommi, P., & Tosti, G. 2006, *A&A*, 448, 861, doi: [10.1051/0004-6361:20053644](https://doi.org/10.1051/0004-6361:20053644)
- Massaro, F., Giommi, P., Tosti, G., et al. 2008a, *A&A*, 489, 1047, doi: [10.1051/0004-6361:200809824](https://doi.org/10.1051/0004-6361:200809824)
- Massaro, F., Tramacere, A., Cavaliere, A., Perri, M., & Giommi, P. 2008b, *A&A*, 478, 395, doi: [10.1051/0004-6361:20078639](https://doi.org/10.1051/0004-6361:20078639)
- Mastichiadis, A., & Kirk, J. G. 1997, *A&A*, 320, 19, <https://arxiv.org/abs/astro-ph/9610058>
- Nalewajko, K. 2013, *MNRAS*, 430, 1324, doi: [10.1093/mnras/sts711](https://doi.org/10.1093/mnras/sts711)
- Nie, J., Fan, J., Yang, R., & Yang, J. 2014, *Science China Physics, Mechanics, and Astronomy*, 57, 2007, doi: [10.1007/s11433-014-5560-8](https://doi.org/10.1007/s11433-014-5560-8)
- Nieppola, E., Valtaoja, E., Tornikoski, M., Hovatta, T., & Kotiranta, M. 2008, *A&A*, 488, 867, doi: [10.1051/0004-6361:200809716](https://doi.org/10.1051/0004-6361:200809716)
- Padovani, P., & Giommi, P. 1995, *MNRAS*, 277, 1477, doi: [10.1093/mnras/277.4.1477](https://doi.org/10.1093/mnras/277.4.1477)
- Paggi, A., Cavaliere, A., Vittorini, V., D'Ammando, F., & Tavani, M. 2011, *ApJ*, 736, 128, doi: [10.1088/0004-637X/736/2/128](https://doi.org/10.1088/0004-637X/736/2/128)
- Paggi, A., Massaro, F., Vittorini, V., et al. 2009, *A&A*, 504, 821, doi: [10.1051/0004-6361/200912237](https://doi.org/10.1051/0004-6361/200912237)
- Rybicki, G. B., & Lightman, A. P. 1979, *Radiative processes in astrophysics*
- Savolainen, T., Homan, D. C., Hovatta, T., et al. 2010, *A&A*, 512, A24, doi: [10.1051/0004-6361/200913740](https://doi.org/10.1051/0004-6361/200913740)
- Sharma, M., Nayak, J., Koul, M. K., et al. 2015, *Nuclear Instruments and Methods in Physics Research A*, 770, 42, doi: [10.1016/j.nima.2014.10.012](https://doi.org/10.1016/j.nima.2014.10.012)
- Shields, G. A. 1978, *Nature*, 272, 706, doi: [10.1038/272706a0](https://doi.org/10.1038/272706a0)
- Tramacere, A., Giommi, P., Perri, M., Verrecchia, F., & Tosti, G. 2009, *A&A*, 501, 879, doi: [10.1051/0004-6361/200810865](https://doi.org/10.1051/0004-6361/200810865)
- Tramacere, A., Massaro, E., & Taylor, A. M. 2011, *ApJ*, 739, 66, doi: [10.1088/0004-637X/739/2/66](https://doi.org/10.1088/0004-637X/739/2/66)
- Ulrich, M.-H., Maraschi, L., & Urry, C. M. 1997, *ARA&A*, 35, 445, doi: [10.1146/annurev.astro.35.1.445](https://doi.org/10.1146/annurev.astro.35.1.445)
- Urry, C. M., & Padovani, P. 1995, *PASP*, 107, 803, doi: [10.1086/133630](https://doi.org/10.1086/133630)



- Ushio, M., Stawarz, L., Takahashi, T., et al. 2010, *ApJ*, 724, 1509, doi: [10.1088/0004-637X/724/2/1509](https://doi.org/10.1088/0004-637X/724/2/1509)
- Wakely, S. P., & Horan, D. 2008, in *International Cosmic Ray Conference*, Vol. 3, *International Cosmic Ray Conference*, 1341–1344
- Wu, Z., Jiang, D. R., Gu, M., & Liu, Y. 2007, *A&A*, 466, 63, doi: [10.1051/0004-6361:20066754](https://doi.org/10.1051/0004-6361:20066754)
- Wu, Z.-Z., Gu, M.-F., & Jiang, D.-R. 2009, *Research in Astronomy and Astrophysics*, 9, 168, doi: [10.1088/1674-4527/9/2/006](https://doi.org/10.1088/1674-4527/9/2/006)
- Xie, G., Dai, B., Liang, E., Ma, L., & Jiang, Z. 2001, *PASJ*, 53, 469, doi: [10.1093/pasj/53.3.469](https://doi.org/10.1093/pasj/53.3.469)
- Yang, J., Fan, J., Nie, J., et al. 2017, *Ap&SS*, 362, 22, doi: [10.1007/s10509-016-3002-y](https://doi.org/10.1007/s10509-016-3002-y)
- Yang, J. H., Fan, J. H., Hua, T. X., & Wu, D. X. 2014, *Ap&SS*, 352, 819, doi: [10.1007/s10509-014-1983-y](https://doi.org/10.1007/s10509-014-1983-y)
- Zhang, J., Liang, E.-W., Zhang, S.-N., & Bai, J. M. 2012, *ApJ*, 752, 157, doi: [10.1088/0004-637X/752/2/157](https://doi.org/10.1088/0004-637X/752/2/157)
- Zhang, J., Xue, Z.-W., He, J.-J., Liang, E.-W., & Zhang, S.-N. 2015, *ApJ*, 807, 51, doi: [10.1088/0004-637X/807/1/51](https://doi.org/10.1088/0004-637X/807/1/51)
- Zhang, Y. T., & Fan, J. H. 2019, *Acta Astronomica Sinica*, 60, 7
- Zheng, Y. G., Kang, S. J., Yang, C. Y., & Bai, J. M. 2019, *ApJ*, 873, 7, doi: [10.3847/1538-4357/ab02fb](https://doi.org/10.3847/1538-4357/ab02fb)
- . 2020, *MNRAS*, 499, 1188, doi: [10.1093/mnras/staa2919](https://doi.org/10.1093/mnras/staa2919)
- Zheng, Y. G., Long, G. B., Yang, C. Y., & Bai, J. M. 2018, *PASP*, 130, 083001, doi: [10.1088/1538-3873/aac7c0](https://doi.org/10.1088/1538-3873/aac7c0)
- Zheng, Y.-G., Yang, C.-Y., Kang, S.-J., & Bai, J.-M. 2021, *Research in Astronomy and Astrophysics*, 21, 008, doi: [10.1088/1674-4527/21/1/8](https://doi.org/10.1088/1674-4527/21/1/8)
- Zheng, Y. G., Yang, C. Y., Zhang, L., & Wang, J. C. 2017, *ApJS*, 228, 1, doi: [10.3847/1538-4365/228/1/1](https://doi.org/10.3847/1538-4365/228/1/1)
- Zhong, W., Liu, W. G., & Zheng, Y. G. 2018, *Ap&SS*, 363, 179, doi: [10.1007/s10509-018-3397-8](https://doi.org/10.1007/s10509-018-3397-8)